

Exploring the Optimal Size of Grid-forming Energy Storage in an Off-grid Renewable P2H System under Multi-timescale Energy Management

Jie Zhu^a, Yiwei Qiu^{a,*}, Yangjun Zeng^a, Yi Zhou^a, Shi Chen^a, Tianlei Zang^a, Buxiang Zhou^a,
Zhipeng Yu^b, Jin Lin^b

^aCollege of Electrical Engineering, Sichuan University, Chengdu, 610065, China

^bDepartment of Electrical Engineering, Tsinghua University, Beijing, 100087, China

Abstract

Utility-scale off-grid renewable power-to-hydrogen systems (OReP2HSs) typically include photovoltaic plants, wind turbines, electrolyzers (ELs), and energy storage systems. As an island system, OReP2HS requires at least one component, generally the battery energy storage system (BESS), that operates for grid-forming control to provide frequency and voltage references and regulate them through transient power support and short-term energy balance regulation. While larger BESS capacity increases this ability, it also raises investment costs. This paper proposes a framework of layered multi-timescale energy management system (EMS) and evaluates the most cost-effective size of the grid-forming BESS in the OReP2HS. The proposed EMS covers the timescales ranging from those for power system transient behaviors to intra-day scheduling, coordinating renewable power, BESS, and ELs. Then, an iterative search procedure based on high-fidelity simulation is employed to determine the size of the BESS with minimal levelized cost of hydrogen (LCOH). Simulations over a reference year, based on the data from a planned OReP2HS project in Inner Mongolia, China, show that with the proposed EMS, the base-case optimal LCOH is 33.212 CNY/kg (4.581 USD/kg). The capital expenditure of the BESS accounts for 17.83% of the total, and the optimal BESS size accounts for 13.6% of the rated hourly energy output of power sources, considering frequency and voltage stability and long-term (8760 h) energy balance. The yearly degradation of battery is 4.87%. Sensitivity analysis reveals that by reducing the electrolytic load adjustment time step from 90 to 5 s and increasing its ramping limit from 1% to 10% rated power per second, the BESS size decreases by 53.57%, and the LCOH decreases to 25.458 CNY/kg (3.511 USD/kg). Considering the cost of designing and manufacturing utility-scale ELs with fast load regulation capability, a load adjustment time step of 5 to 10 s and a ramping limit of 4–6% rated power per second are recommended to balance profitability and technological feasibility.

Keywords: Off-grid power to hydrogen, green hydrogen, energy management system, battery energy storage system, levelized cost of hydrogen

*Corresponding author

Email address: ywqiu@scu.edu.cn (Yiwei Qiu)

1. Introduction

1.1. Background and Motivation

In the global effort to reduce carbon emissions, particularly in the electrical power, energy, transport, and chemical sectors, renewable power-to-hydrogen (ReP2H) technology has emerged as a promising solution. According to the *China's Hydrogen Development Strategy* [1], the installed capacity of hydrogen electrolyzers (ELs) in China reached 1.4 GW by 2022. Projections indicate this will increase to 100 GW in China and 35 GW in Europe by 2030, with 80% of hydrogen demand met through ReP2H [2].

Utility-scale ReP2H systems can be grid-connected or off-grid. Grid-connected systems can maintain steady hydrogen production by exchanging power with the utility grid to manage renewable power fluctuations. However, ensuring all hydrogen produced meets green certification is challenging [3, 4], and remote areas with abundant renewable resources, such as islands and deserts, often lack grid access. Conversely, off-grid ReP2H systems (OReP2HS) can be designed flexibly based on the spatial distribution of the renewable energy resources. The stringent constraints and regulations on power exchange with the utility grid are also avoided. Benefiting from these advantages, off-grid ReP2H has gained policy support, leading to many demonstration projects under construction [5–7].

The OReP2HS typically comprises photovoltaic (PV) plants, wind turbines (WTs), ELs, and a battery energy storage system (BESS) [8]. Alternating current (AC) paradigms are often preferred due to the immature market for direct current (DC) grid equipment [9, 10]. In the off-grid mode, at least one component in the OReP2HS must operate under grid-forming control (such as V/F droop and virtual synchronous generator control) to provide frequency and voltage references and regulate them through transient power support and short-term energy balance regulation. However, the development of grid-forming capabilities for WTs, PVs, and ELs is still in the experimental stage [11–13]. Using BESS as the grid-forming component appears to be the most feasible solution [14, 15], but poses challenges in balancing economy and safety.

First, if the imbalanced power exceeds the limits of the grid-forming BESS, the OReP2HS loses its frequency and voltage references, leading to instantaneous instability [16, 17]. A large BESS capacity and a high charging/discharging rate enhance stability but also increase investment costs. Therefore, finding the optimal trade-off between economy and stability is crucial for sizing the BESS in an OReP2HS. Second, ELs have a wide load range and low-latency response capability [18]. A proper design of a controller that enables efficient electrolytic load regulation is essential for reducing BESS capacity requirements and, consequently, the levelized cost of hydrogen (LCOH).

These challenges highlight the need for an energy management system (EMS) to coordinate PVs, WTs, BESS, and ELs for stable OReP2HS operation while improving profitability. To address these issues, this research proposes a comprehensive multi-timescale EMS, covering power system transient behaviors to intra-day rolling scheduling. Using high-fidelity models, the BESS size is evaluated for minimal LCOH while

considering stability and year-long energy balance, and the factors influencing the BESS size are analyzed. Section 1.2 provides a brief literature review, and the contributions of this work are summarized in Section 1.3.

1.2. Literature Review

An EMS plays a fundamental role in the design, planning, and operation of the OReP2HS. Therefore, this topic has attracted global research attention.

Some studies proposed a rule-based EMS and conducted year-long production simulations of the OReP2HS. Metaheuristic algorithms are then employed to optimize the sizes of the system components. For example, Marocco et al. [19–21] designed a rule-based EMS for an OReP2HS to maintain energy autonomy in remote microgrids. When renewable power exceeds load demand, the BESS is charged first. Once the BESS reaches its maximum state of charge (SOC), ELs are started up, and surplus power is directed to hydrogen production. The capacities of PVs, WTs, BESS, ELs, and hydrogen tanks (HTs) are optimized using particle swarm optimization (PSO) with hourly time resolution [20]. A techno-economic analysis, considering the degradation cost of batteries and fuel cells, is presented in [21]. Gandiglio et al. [22] assessed the environmental benefits of powering an island village with an OReP2HS using the EMS proposed in [19]. Abdulrahman et al. [23] used a similar OReP2HS to produce hydrogen for refueling hydrogen-based vehicles in an off-grid residential area in Dhahran, Saudi Arabia. A year-long production simulation with hourly time resolution obtained a minimal LCOH of 36.32 USD/kg.

The OReP2HS also plays a crucial role in achieving energy autonomy for green buildings [24], standalone communities [25, 26], and off-grid industrial parks [27]. The system sizes are optimized using PSO [24], charged system search algorithms [25], genetic algorithms [26], and gray wolf optimization [26], as well as NSGA-II [27] based on rule-based EMSs.

Other researchers designed mathematical optimization-based EMSs for the OReP2HS and determined component sizes through deterministic optimization. Day-ahead/intra-day optimal scheduling was considered for production simulations. Oyewole et al. [28] proposed a mixed-integer linear programming (MILP) approach for designing OReP2HS in insular communities. Linear programming (LP) was utilized for planning an OReP2HS to supply a research facility in isolated regions [29]. For transportation and industrial applications, Wang et al. [30] focused on green hydrogen production for green ammonia synthesis, employing MILP for simulations and optimizations. Ibagon et al. [31] investigated the optimal size of OReP2HS for export-oriented green hydrogen production in Uruguay, using sequential quadratic programming (SQP) and predicting a decrease in LCOH from 3.5 USD/kg to 2.3 USD/kg by 2030 with technological maturity. Yang et al. [32] designed an off-grid hydrogen supply chain in Fujian, China, using chance-constrained programming to address planning and operation problems. Shao et al. [33] proposed bi-level stochastic programming for dispatch and size determination of OReP2HS, while Pang et al. [34] suggested a similar

Table 1: Summary of the literature related to the planning and designing of OReP2HS

Literature	Components	8760-hour energy balance	Day-ahead/Intra- day scheduling	Frequency/ voltage security	Resolution of simulation	Method/ Software
[19] (2020), [21] (2022), [22] (2021)	PV/WT/BT ¹ / EL/HT	✓			1 h	Iterative searching
[23] (2022)	PV/WT/BT/EL	✓			1 h	Iterative searching
[20] (2022), [24] (2023)	PV/WT/BT/ EL/HT	✓			1 h	PSO
[26] (2020)	PV/WT/SC ² / EL/HT/ Micro-hydro plant	✓			1 h and 1 month	Metaheuristic
[27] (2020)	PV/WT/EL/HT/	✓			1 h	NSGA-II
[28] (2024)	PV/WT/EL/HT	✓	✓		1 h	MILP
[29] (2023)	PV/WT/BT/ EL/HT/DG ³	✓	✓		1 h	LP
[30] (2023)	PV/WT/BT/EL/	✓	✓		1 h	MILP
[31] (2023)	PV/WT/BT/EL	✓	✓		1 h	SQP
[32] (2020)	PV/WT/BT/EL	✓	✓		1 h	Chance constrained programming
[33] (2023)	PV/WT/BT/ EL/HT	✓	✓		1 h	Stochastic programming
[34] (2022)	PV/WT/BT/ EL/Dispenser	✓	✓		1 h	MIQCP
[35] (2022), [36] (2022), [37] (2017)	PV/WT/BT/ EL/HT	✓	✓		1 h	HOMER
[38] (2024)	PV/WT/BT/EL	✓	✓		1 h	HOMER Pro
[39] (2023)	PV/WT/BT/ EL/HT	✓	✓		1 h	DECAPLA
[40] (2022)	PV/WT/BT/EL	✓			5 min	PSO
[41] (2023)	PV/WT/BT/EL	✓			5 min	Metaheuristic
[42] (2023)	WT/EL	✓			5 min	Iterative searching
This work	PV/WT/BT/EL	✓	✓	✓	0.04 ms to 4 h	High-fidelity simulation-based searching

¹Battery; ²Super capacitor; ³Diesel generator.

bi-layer framework using mixed integer quadratic constrained programming (MIQCP) for scheduling.

Commercial planning software has also been used to design OReP2HS, often integrating MILP-based EMS. Babaei et al. [35] used OReP2HS to supply power to energy-stressed islands in Eastern Canada, employing HOMER to find the most cost-effective configuration. Abdin et al. [38] used HOMER PRO to optimize the sizes of PV, WTs, ELs, HTs, and BESS. Similarly, HOMER/HOMER PRO was used to find cost-effective configurations of OReP2HS in remote communities [36] and villages [37]. DECAPLA was applied for simulation in the design of OReP2HS for independent communities, considering an MILP-based EMS [39].

Most studies have considered hourly time resolution for designing the EMS in the OReP2HS, overlooking renewable power fluctuations on shorter timescales. Nevertheless, some studies have employed more refined

time resolution. Ibáñez-Rioja et al. [40, 41] used 300-second-resolution data from a Finnish wind farm for OReP2HS production simulations, obtaining a more precise LCOH of 2 Euro/kg by 2030 in southeastern Finland. Zheng et al. [42] used 5-minute-resolution data to evaluate the LCOH for an off-grid wind power-to-hydrogen system, finding an LCOH range of 1.66–13.61 USD/kg in wind-rich areas in China and Denmark.

The reviewed studies reported in the literature have mainly focused on the long-term energy balance and scheduling of the OReP2HS with 5-minute to hourly time resolution, as summarized in Table 1. These studies consider only the power balance at each time step, neglecting the dynamic interactions of the control loops of PV, WTs, BESS, and ELs. This results in two shortcomings in planning and operating the OReP2HS: the underutilization of the EL load regulation capacity and the neglect of voltage and frequency stability.

Many researchers have investigated the use of ELs for frequency regulation in the power grid [43–45], demonstrating the capability of the ELs for load regulation within seconds. This capability can smooth renewable power fluctuations in OReP2HS, reducing BESS capacity requirements. However, this second-level capability is not considered in existing works with 5-minute or hourly resolution, leading to a potential overestimation of the optimal BESS size. Therefore, a high-resolution EMS for OReP2HS is needed.

Moreover, in the absence of grid energy support, voltage and frequency stability are critical issues for the OReP2HS. Grid-forming control, typically implemented in BESS, thus becomes essential [46]. It provides necessary frequency and voltage references for OReP2HS and adjusts output power instantaneously to maintain stability. If the power imbalance exceeds the BESS capacity, the OReP2HS may destabilize immediately or shut down due to the loss of references [47]. This process occurs on the time scale of milliseconds and involves complex interactions among the PV, WT, BESS, and EL control loops. Simulations reported in the literature reviewed in Table 1, with minute to hourly resolution, cannot reveal the system stability, risking the underestimation of the BESS requirements and erroneous estimation of LCOH. Thus, the LCOH ranges of 1.6–3.5 USD/kg reported in the literature [31, 40–42] appear to be overly optimistic.

1.3. Contributions

To fill the aforementioned gaps, this paper proposes a hierarchical EMS that considers a wide range of behaviors from power system transient behaviors to production scheduling. We establish a comprehensive model to conduct high-fidelity production simulations and evaluate the most cost-effective size for the grid-forming BESS and the levelized cost of hydrogen (LCOH). The main contributions of this research obtained using an OReP2HS planned in Inner Mongolia, China as a case study are summarized as follows:

1. A hierarchical EMS is proposed for the OReP2HS, covering a range of behaviors from transient power balance to intra-day scheduling (time resolution scales from milliseconds to hours). It includes MILP-based rolling scheduling, load-following control, and an emergency handling strategy to address contingencies such as WT/PV/EL tripping.

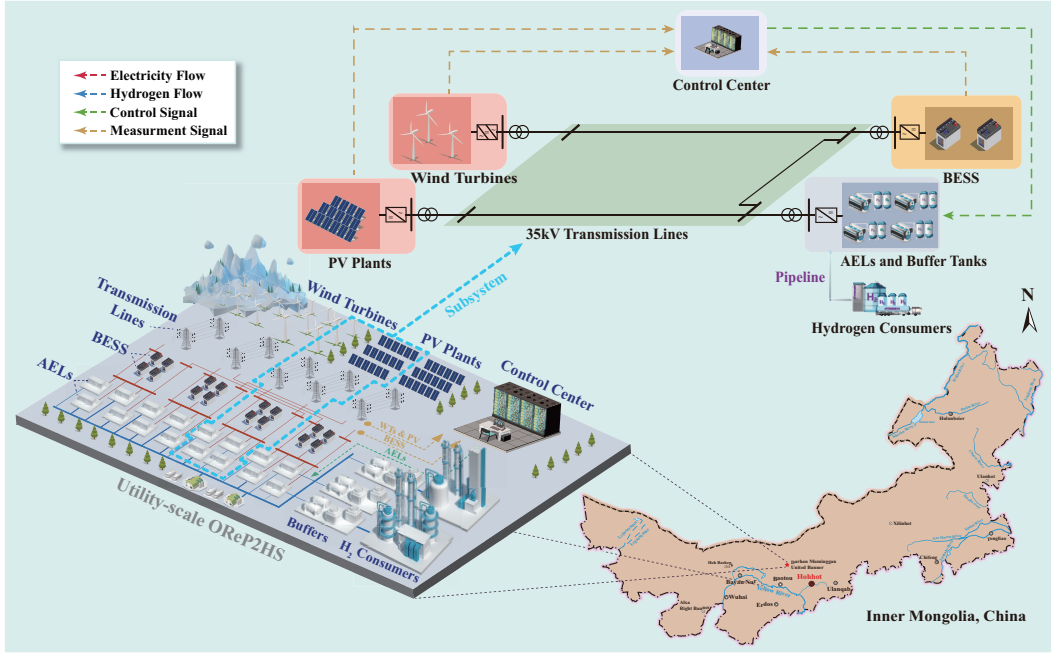


Figure 1: Schematic diagram of the studied OReP2HS located in Inner Mongolia, China.

2. A comprehensive model is developed to support the high-fidelity production simulation of the OReP2HS. This model integrates the EMS with electromagnetic transient simulation models, considering the dynamic behaviors of PV, WTs, ELs, and BESS, as well as frequency and voltage stability.
3. The optimal size of the grid-forming BESS is evaluated through iterative searching to achieve minimal LCOH. Constraints for long-term (8760 h) energy balance, frequency and voltage stability, and continuous operation under emergency conditions are simultaneously considered for the first time.
4. The impact of the proposed EMS on the optimal BESS size and LCOH is assessed. The findings indicate that the base-case optimal BESS size and LCOH for the off-grid application are 6.8 MW/3.4 MWh and 33.212 CNY/kg (4.581 USD/kg). They can be further reduced by improving load ramping capability and shortening the time steps for electrolytic load adjustments.

The rest of this paper is organized as follows. The configuration and component model of the OReP2HS are presented in Section 2. In Section 3, the hierarchical EMS is described in detail. Section 4 presents the method for evaluating the optimal BESS size. The results and sensitivity analysis are given in Section 5. Finally, Section 6 presents the conclusion and future prospects.

2. System Description

2.1. Configuration of the OReP2HS

The OReP2HS studied in our research is based on a realistic project planned in Inner Mongolia, China. Its schematic diagram is shown in Fig. 1. This utility-scale OReP2HS comprises multiple sub-systems that are electrically independent. The produced hydrogen is collected by pipelines and fed to industrial consumers in a chemical park.

This paper takes one subsystem as the research object. It is planned to install three 6.25 MW wind turbines (WTs) from *Goldwind Sci & Tech* and a 6.25 MWp photovoltaic (PV) plant from *LONGi Green Energy Technology*. The hydrogen production plant comprises three alkaline ELs (AELs) from *Peric Hydrogen Technologies*. Each AEL has a rated power of 5 MW and a maximum overload of 20% of the rating. A battery energy storage system (BESS) is taken as the grid-forming equipment, and the evaluation of its size, characterized by the battery capacity and charging/discharging rate, is the goal of this work. All devices are connected by 35 kV AC transmission lines and operate at a rated frequency of 50 Hz.

2.2. Requirements for Sizing the Grid-forming BESS

The size of the grid-forming BESS should meet the stability requirements of the OReP2HS while balancing economic profitability and stability. The following requirements must be satisfied:

1. **Grid-forming ability:** The BESS must provide frequency and voltage references and offer transient power support to maintain these within limits. This is a prerequisite for the stable operation of an OReP2HS. While increasing battery capacity and charging/discharging rates enhances grid-forming ability, it also raises investment, operation, and maintenance costs.
2. **Continuous operation during emergencies:** The OReP2HS must immediately balance power shortages or surpluses to maintain frequency and voltage stability during emergencies, such as the tripping of a WT, PV, or EL. This capability aims to avoid unnecessary blackouts and ensure a reliable hydrogen supply.
3. **Long-term energy balance:** The OReP2HS must coordinate PV, WTs, BESS, and ELs to maintain year-long (8760 h) energy balance while avoiding the BESS being fully charged/discharged to maintain the power regulation ability. Note that under an effective load scheduling strategy, the regulation range of electrolytic load is far beyond that of the BESS. A full utilization of this capability can reduce the size of the BESS and the LCOH.

The grid-forming ability and continuous operation during emergencies involve complex dynamic interactions between PV, WTs, BESS, and ELs. A refined simulation model is necessary to test these interactions. On the other hand, when testing long-term energy balance, a trade-off between time efficiency and accuracy is needed, making simplified models more suitable. Therefore, we develop both refined and simplified

simulation models in Section 2.3. Then, a multi-timescale EMS is presented in Section 3 to support the simulations.

2.3. Simulation Models of the OReP2HS

Refined and simplified simulation models are developed to test the three requirements listed in Section 2.2. These models are derived from real-world devices as introduced in Section 2.1 and are described below. Detailed topologies, controllers, and parameters are presented in Appendix A.

The refined model is developed in the electromagnetic transient form and established in *Matlab/Simulink*. For WTs and the PV plant, maximum power point tracking (MPPT) control is integrated into the control loops. The influence of the ambient temperature on the PV plant output is also considered. For the AELs, detailed models considering electrolysis stacks and rectifiers are developed. The rectifier includes vector-orientation-controlled IGBT-PWM-based AC/DC and Buck/Boost-based DC/DC converters. The stack is modeled as an equivalent circuit of a nonlinear resistance in series with a counter electromotive force to simulate its U-I feature [48]. The grid-forming BESS adopts voltage/frequency (V/F) droop control. A generic model represents the battery as a controllable ideal DC source with an equivalent resistance [49].

The simplified model has the same topologies and parameters as the refined model but differs with regard to power electronic converters modeling. In the refined model, converters are modeled with detailed circuit topology and switching dynamics of the IGBT/diode pairs controlled by PWM signals. For the simplified model, the switching dynamics within the converters are neglected. Instead, a switching-function model directly controlled by the reference voltage signals [50] is used to improve efficiency in testing long-term balance.

3. Multi-timescale Energy Management System

3.1. Framework

The framework of the proposed multi-timescale EMS is illustrated in Fig. 2. WTs and the PV plant operate with the built-in MPPT controllers. The grid-forming BESS operates under V/F droop control to provide voltage and frequency references. The control center regulates the electrolytic load to track the renewable power.

The timescale of the proposed EMS covers the range from 0.04 ms to 4 h, and four sub-strategies are included. The strategies are coordinated to achieve stable and economic operation of the OReP2HS.

1. **Rolling Scheduling (from 5 min to 4 h):** The rolling scheduling (RS) aligns the hydrogen production plan with the renewable generation profile based on forecasts. It utilizes an MILP to determine the start-up/shut-down/standby states and baseline load for each EL in every upcoming 4 h. Its time step is typically from 5 to 15 min.

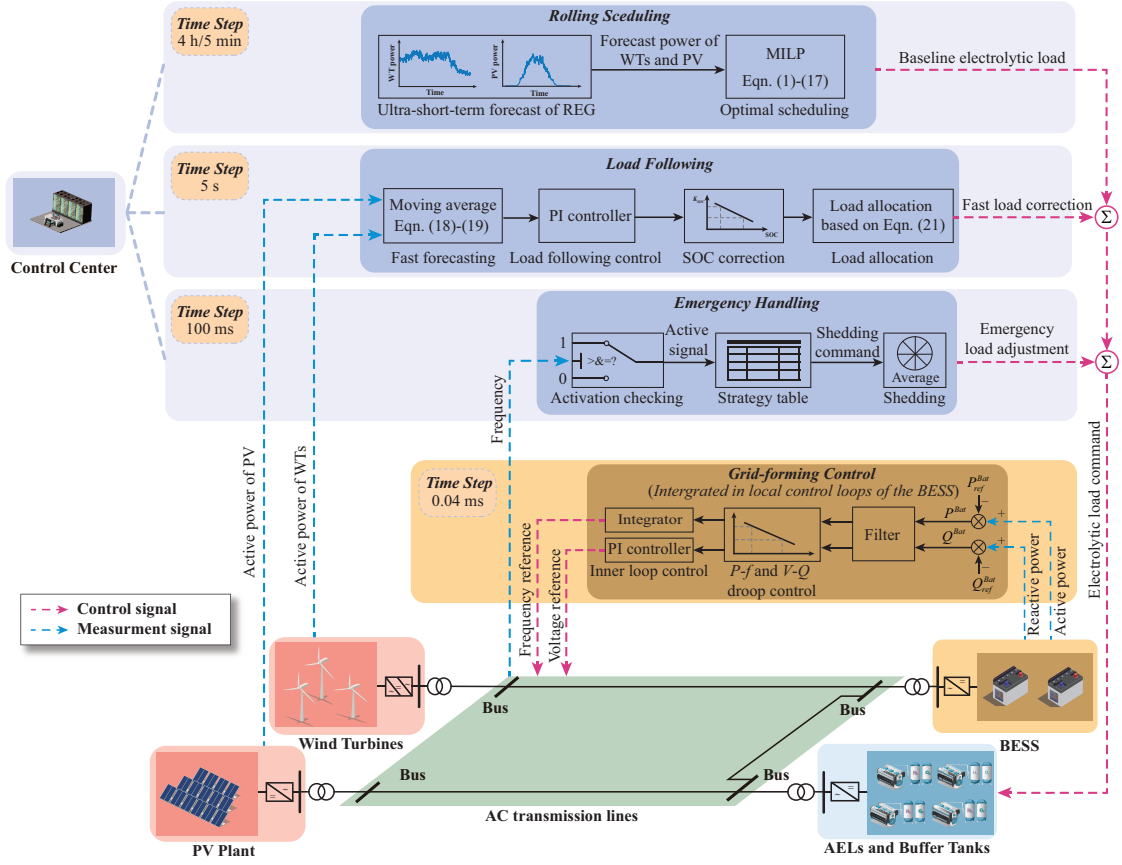


Figure 2: Framework of the proposed multi-timescale EMS.

2. **Load Following (typically 5 s):** The load following (LF) is similar to automatic generation control (AGC) in power systems. It adjusts the load of AELs every 5 s. The goal is to ensure that the electrolytic load closely tracks the renewable power, thereby reducing the regulation demand on the grid-forming BESS.
3. **Emergency Handling (100 milliseconds):** The emergency handling (EH) ensures the continuous operation of the OReP2HS during emergencies. It monitors system frequency and power balance and adjusts the power of PV, WTs, BESS, and ELs in the event of contingencies, such as WT/PV/EL tripping.
4. **Grid-forming Control (0.04 milliseconds):** Under grid-forming control, the BESS provides frequency and voltage references in the electrical network, offering transient power support and energy balance regulation to maintain stability.

3.2. Rolling Scheduling

The RS module determines the operational states (start-up, shut-down, standby) and baseline load of each EL based on ultra-short-term forecasts of renewable power for the upcoming 4 h. This module uses a

Mixed-Integer Linear Programming (MILP) approach with a time step of 5 to 15 min. The objective is to maximize hydrogen production revenue, as described by:

$$\min_{\mathbf{x}} \sum_{t=0}^{T_{RS}} \sum_{i=1}^n \{(-C^{H_2} q_t^{H_2}) \Delta t_{RS} + C_{up,h}^{EL} \mu_{i,t}^{up,h} + C_{up,c}^{EL} \mu_{i,t}^{up,c} + C_{down}^{EL} \mu_{i,t}^{down} + s(\sum_{l=1}^m \hat{P}_{l,t}^{WT,cut} + \hat{P}_t^{PV,cut}) \Delta t_{RS}\}, \quad (1)$$

where \mathbf{x} represents the decision variables, including the operational states and load power of ELs; m and n are the number of WTs and ELs, respectively; $C^{H_2} q_t^{H_2} \Delta t_{RS}$ is the revenue of selling hydrogen; $C_{up,h}^{EL} \mu_{i,t}^{up,h} + C_{up,c}^{EL} \mu_{i,t}^{up,c} + C_{down}^{EL} \mu_{i,t}^{down}$ represent the cost of state transition of an EL; $s(\sum_{l=1}^m \hat{P}_{l,t}^{WT,cut} + \hat{P}_t^{PV,cut}) \Delta t_{RS}$ represents the penalty for curtailing renewable power.

The state transition and constraints of the electrolytic load of the ELs under different states can be expressed as follows [18, 51, 52]:

$$\mu_{i,t}^{st} + \mu_{i,t}^{sb} + \mu_{i,t}^{sp} = 1, \quad (2)$$

$$\mu_{i,t}^{down} = \mu_{i,t-1}^{st} \mu_{i,t}^{sp}, \quad (3)$$

$$\mu_{i,t}^{up,h} = \mu_{i,t-1}^{sb} \mu_{i,t}^{st}, \quad (4)$$

$$\mu_{i,t}^{up,c} = \mu_{i,t-1}^{sp} \mu_{i,t}^{st}, \quad (5)$$

$$T_{min}^{down} \mu_{i,t}^{down} \leq \sum_{t}^{t-1+T_{min}^{down}} \mu_{i,t}^{sp}, \quad \forall t \leq T_{RS} + 1 - T_{min}^{down}, \quad (6)$$

$$\mu_{i,t}^{sb} P_{sb}^{EL} + \mu_{i,t}^{st} r_{min}^{EL} S_i^{EL} \leq P_{i,t}^{EL,RS} \leq \mu_{i,t}^{st} r_{max}^{EL} S_i^{EL} + \mu_{i,t}^{sb} P_{sb}^{EL}. \quad (7)$$

where $\mu_{i,t}^{st}$, $\mu_{i,t}^{sb}$, and $\mu_{i,t}^{sp}$ are binary variables indicating the production, standby, and shut-down states of the ELs, respectively; (6) represents the minimal time interval between shut-down and start-up, where T_{min}^{down} is set at 1 h; $P_{i,t}^{EL,RS}$ is the load of the ELs; P_{sb}^{EL} is the power consumption in standby state; S_i^{EL} is the capacity of a single EL; r_{min}^{EL} and r_{max}^{EL} are ramping limits.

The relationship between hydrogen production and electricity consumption is nonlinear and is influenced by the temperature and pressure of ELs. In this section, to ensure real-time computing, the relationship between the electrolytic power $P_{i,t}^{EL,RS}$ and hydrogen production $q_{i,t}^{H_2}$ is described using a fixed electricity consumption coefficient $k_i^{H_2}$ following the typical approach used in the previous work [19–21, 28, 29]:

$$(1 - \mu_{i,t}^{sb}) P_{i,t}^{EL,RS} = k_i^{H_2} q_{i,t}^{H_2}. \quad (8)$$

It is important to note that different from the use of a linear model described here, a nonlinear curve of hydrogen production and electricity consumption derived from a commercial AEL produced by *Peric Hydrogen Technologies* is employed to ensure accuracy for BESS size optimization and LCOH evaluation in Section 4.

In addition to the ELs, energy shifting regulation is also provided by the BESS. The constraints for the

BESS are listed as follows:

$$SOC_t^{\text{BES}} = SOC_0^{\text{BES}} + \sum_{i=1}^{T_{\text{RS}}} (\eta^{\text{BES}} P_t^{\text{BES,C}} - P_t^{\text{BES,D}} / \eta^{\text{BES}}) \Delta t_{\text{RS}}, \quad (9)$$

$$|SOC_{T_{\text{RS}}}^{\text{BES}} - SOC_0^{\text{BES}}| \leq 0.05, \quad (10)$$

$$SOC_{\min}^{\text{BES}} \leq SOC_t^{\text{BES}} \leq SOC_{\max}^{\text{BES}} \quad (11)$$

$$0 \leq P_t^{\text{BES,C}} \leq \mu_t^{\text{BES,C}} P_t^{\text{BES,Cmax}}, \quad (12)$$

$$0 \leq P_t^{\text{BES,D}} \leq \mu_t^{\text{BES,D}} P_t^{\text{BES,Dmax}}, \quad (13)$$

$$0 \leq \mu_t^{\text{BES,C}} + \mu_t^{\text{BES,D}} \leq 1, \quad (14)$$

where (9) is the state of charge (SOC) of the BESS; η^{BES} is charging/discharging efficiency; $P_t^{\text{BES,C}}$ and $P_t^{\text{BES,D}}$ represent the charging and discharging power, respectively; the final constraints (12)–(14) prevent the BESS from charging and discharging simultaneously; and $\mu_t^{\text{BES,C}}$ and $\mu_t^{\text{BES,D}}$ are binary variables.

The balance of power for each time step in the RS is finally required, and is described by:

$$\sum_{l=1}^m \hat{P}_{l,t}^{\text{WT}} - \hat{P}_t^{\text{PV}} - \sum_{l=1}^m \hat{P}_{l,t}^{\text{WT,cut}} + \hat{P}_t^{\text{PV,cut}} + P_t^{\text{BES,D}} = P_t^{\text{BES,C}} + \sum_{i=1}^n P_{i,t}^{\text{EL,RS}}, \quad (15)$$

$$0 \leq \hat{P}_{l,t}^{\text{WT,cut}} \leq \hat{P}_{l,t}^{\text{WT}}, \text{ for } l = 1, \dots, m, \quad (16)$$

$$0 \leq \hat{P}_t^{\text{PV,cut}} \leq \hat{P}_t^{\text{PV}}, \quad (17)$$

where $\hat{P}_{l,t}^{\text{WT,cut}}$ and $\hat{P}_t^{\text{PV,cut}}$ are the power curtailments of WT and PV, respectively.

Finally, we summarize (1)–(17) to establish the MILP-based RS model. This model is similar to those used in the previous studies for ReP2HS planning [28, 30–33] and can be easily solved by off-the-shelf solvers. However, while prior works only consider intra-day scheduling (as discussed in Section 1.2), we further investigate the influence of seconds-level load control of the AELs (Section 3.3) and the grid-forming control of the BESS at the millisecond scale (Section 3.5) on the sizing of the BESS.

3.3. Load Following

The LF module adjusts the load of each EL in real time. It aims to optimize the load regulation capacity of ELs to balance power within seconds. This module includes *fast forecasting*, *load following control*, *SOC correction*, and *load allocation*, as shown in Fig. 2.

The fast forecasting sub-module predicts renewable power for the next few seconds (determined by Δt_{LF}) using a discrete moving average (MA) process, as shown in (18). It uses real-time active power measurement from WTs and the PV plant to generate the load correction command P_t^{LF} according to (19).

$$\hat{P}_t^{\text{RES}} = \alpha \hat{P}_{t-\Delta t_{\text{LF}}}^{\text{RES}} + (1 - \alpha) \frac{1}{q_{\text{LF}}} \sum_{k=1}^{q_{\text{LF}}} \left(\sum_{l=1}^m P_{l,t-k\Delta t_{\text{LF}}}^{\text{WT}} + P_{t-k\Delta t_{\text{LF}}}^{\text{PV}} \right), \quad (18)$$

$$P_t^{\text{LF}} = \hat{P}_t^{\text{RES}} - \sum_{i=1}^n P_{i,t-\Delta t_{\text{LF}}}^{\text{EL}}, \quad (19)$$

where \hat{P}_t^{RES} is the forecasted renewable power; q_{LF} and α are the order and smoothing coefficient of the MA process, set at 4 and 0.6, respectively; Δt_{LF} is the LF time step, typically on the order of seconds (the effect of Δt_{LF} on the EMS performance is discussed in Section 5.3).

The load-following sub-module tracks P_t^{LF} using a PI controller, followed by the use of a SOC correction control sub-module to prevent battery over-charging/discharging. The total correction $P_t^{\text{LF,ref}}$ is given by:

$$P_t^{\text{LF,ref}} = K_{\text{SOC}}(K_{\text{P}}P_t^{\text{LF}} + \int_0^t K_{\text{I}}P_s^{\text{LF}} ds) + \beta, \quad (20)$$

where K_{SOC} and β are constant coefficients, and K_{P} and K_{I} are the proportional and integral gains of the PI controller, respectively.

The allocation of $P_t^{\text{LF,ref}}$ to each EL is based on their adjustable capacity, as shown in (21). If $P_t^{\text{LF,ref}} \geq 0$, indicating a need to increase the electrolytic load, it is distributed based on the upward regulation capacities of ELs, and vice versa for a decrease in the load.

$$P_{i,t}^{\text{EL,LF}} = \begin{cases} \frac{S_i^{\text{EL}} - P_{i,t}^{\text{EL}}}{\sum_{i=1}^n (S_i^{\text{EL}} - P_{i,t}^{\text{EL}})} \times P_t^{\text{LF,ref}}, & \text{for } P_t^{\text{LF,ref}} \geq 0, \\ \frac{-P_{i,t}^{\text{EL}}}{\sum_{i=1}^n P_{i,t}^{\text{EL}}} \times P_t^{\text{LF,ref}}, & \text{for } P_t^{\text{LF,ref}} < 0. \end{cases} \quad (21)$$

Finally, the load reference commands sent to each EL are described by:

$$P_{i,t}^{\text{EL}} = P_{i,t}^{\text{EL,RS}} + P_{i,t}^{\text{EL,LF}}, \quad (22)$$

where $P_{i,t}^{\text{EL,RS}}$ is the baseline load of the i -th EL determined by the RS module presented in Section 3.2 that is updated every Δt_{RS} ; and $P_{i,t}^{\text{EL,LF}}$ is the real-time correction command given by (21) that is updated every Δt_{LF} .

3.4. Emergency Handling

In emergencies, such as the tripping of a WT, PV plant, or EL, a common $N-1$ fault in power systems, the stability of the OReP2HS relies heavily on the grid-forming BESS for rapid power support and prevention of unnecessary blackouts. However, continuous reliance on the BESS during these emergencies can deplete its energy reserves, therefore increasing the required BESS capacity and, consequently, the investment costs. To address this, we propose an Emergency Handling (EH) strategy that coordinates WTs, PV, and ELs to reduce the energy demand on the BESS during emergencies.

The procedure for EH is outlined below. First, it estimates the imbalanced power through system frequency and then regulates the BESS along with PV/WTs/ELs. The severity of the emergency is assessed using the Rate of Change of Frequency (RoCoF) and maximal frequency deviation. When EH is activated, a power shedding command is dispatched to the renewable power sources or electrolytic loads, depending on whether the power loss originated from the load or source side. This is based on a lookup table (see

Table 2: Load/Generation shedding command and activation criteria of the EH

Interval	Load/Generation shedding	Activation criteria (Hz and Hz/s)
SE6	6 MW	$f_t^{\text{PCC}} \leq 49.65$ and $df_t^{\text{PCC}}/dt \leq -11.5$ $f_t^{\text{PCC}} \geq 50.35$ and $df_t^{\text{PCC}}/dt \geq 11.5$
SE5	5 MW	$49.70 \leq f_t^{\text{PCC}} < 49.65$ and $-11.5 < df_t^{\text{PCC}}/dt \leq -10.0$ $50.30 \leq f_t^{\text{PCC}} < 50.35$ and $10.0 \leq df_t^{\text{PCC}}/dt < 11.5$
SE4	4 MW	$49.75 \leq f_t^{\text{PCC}} < 49.70$ and $-10.0 < df_t^{\text{PCC}}/dt \leq -8.0$ $50.25 \leq f_t^{\text{PCC}} < 50.30$ and $8.0 \leq df_t^{\text{PCC}}/dt < 10.0$
SE3	3 MW	$49.80 \leq f_t^{\text{PCC}} < 49.75$ and $-8.0 < df_t^{\text{PCC}}/dt \leq -6.5$ $50.20 \leq f_t^{\text{PCC}} < 50.25$ and $6.5 \leq df_t^{\text{PCC}}/dt < 8.0$
SE2	2 MW	$49.85 \leq f_t^{\text{PCC}} < 49.80$ and $-6.5 < df_t^{\text{PCC}}/dt \leq -4.5$ $50.15 \leq f_t^{\text{PCC}} < 50.20$ and $4.5 \leq df_t^{\text{PCC}}/dt < 6.5$
SE1	1 MW	$49.85 \leq f_t^{\text{PCC}} < 49.80$ and $-4.5 < df_t^{\text{PCC}}/dt \leq -2.5$ $50.15 \leq f_t^{\text{PCC}} < 50.20$ and $2.5 \leq df_t^{\text{PCC}}/dt < 4.5$

Table 2 tailored for the system shown in Fig. 1). The ELs or generators respond to the power shedding command with maximal ramping, reducing the power support demand from the BESS. This facilitates rapid restoration of power balance within the OReP2HS, potentially reducing BESS investment costs.

Notably, for EH activation, both RoCoF and maximal frequency deviation must fall within predefined intervals specified in Table 2. If either indicator falls outside these intervals, EH cannot be activated; if both fall outside all intervals, EH is deactivated.

3.5. V/F Droop-based Grid-forming Control

The V/F droop-based grid-forming control is integrated into the built-in controller of the BESS. It enables the BESS to actively provide frequency and voltage references to the OReP2HS, and its operating principle is described in (23)–(24) [46, 47]. However, implementation of grid-forming control in a BESS is a complex task that requires coordination among the outer V/F droop control, inner current control, measurement, filter, and PWM generator [46]. This procedure involves interactions between different control loops on the ms time scale, necessitating the use of an electromagnetic transient simulation model, as described in detail in Sections 2.3 and Appendix A.

$$\omega_{\Delta t_{\text{sim}}} = \omega_{\Delta t_{\text{sim}}}^{\text{ref}} + K_f(P_{\Delta t_{\text{sim}}}^{\text{BES,ref}} - P_{\Delta t_{\text{sim}}}^{\text{BES}}), \quad (23)$$

$$V_{\Delta t_{\text{sim}}} = V_{\Delta t_{\text{sim}}}^{\text{ref}} + K_v(Q_{\Delta t_{\text{sim}}}^{\text{BES,ref}} - Q_{\Delta t_{\text{sim}}}^{\text{BES}}), \quad (24)$$

where Δt_{sim} is the time step of the electromagnetic transient simulation, typically on the order of milliseconds; ω_t and ω_t^{ref} are the angular frequency ($\omega_t = 2\pi f_t$) and its reference; V_t and V_t^{ref} are the voltage at the point of common connection (PCC) and its reference; and K_f and K_v are droop coefficients, representing the frequency and voltage variation w.r.t. the difference between the instantaneous outputs of the BESS

$P_t^{\text{BES}}/Q_t^{\text{BES}}$ and its setpoint $P_t^{\text{Bat,ref}}/Q_t^{\text{Bat,ref}}$. A comprehensive introduction to grid-forming control can be found in [47].

4. Optimally Sizing the BESS

As mentioned in Section 2.2, sizing the grid-forming BESS involves testing the grid-forming capability, continuous operation during emergencies, and long-term energy balance. These constraints involve complex interactions between WTs, PV plant, ELs, and the BESS, making explicit quantification extremely difficult. Existing methods, such as those in [28–33] that use convex optimization to find the optimal BESS size, are not applicable. Therefore, we employ a high-fidelity production simulation-based iterative searching procedure, based on the proposed multi-timescale EMS, to evaluate the most cost-effective BESS size. The iterative search procedure is illustrated in Fig. 3, with the objective and constraints described below.

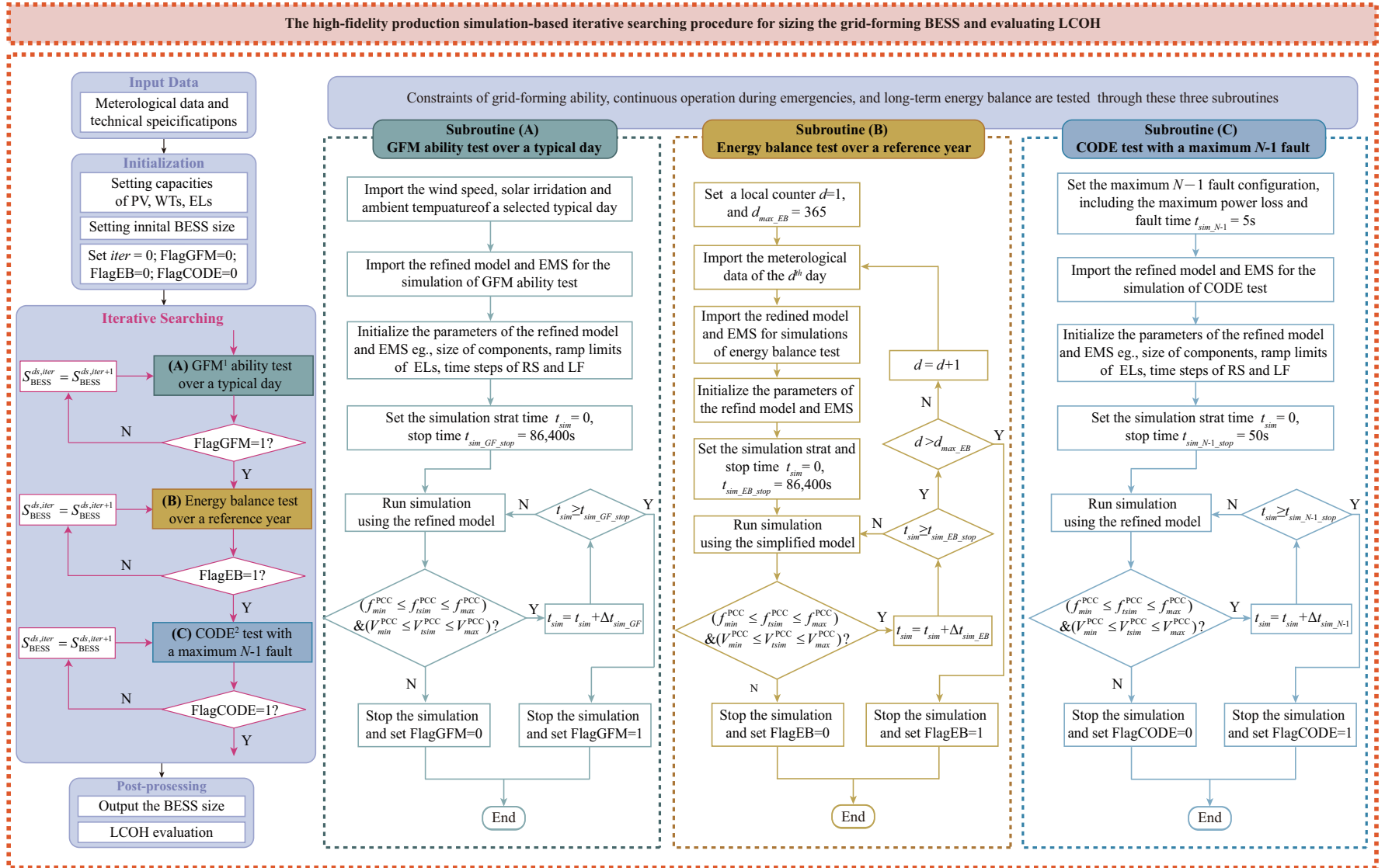
¹GFM: Grid-forming; ²CODE: Continuous operation under emergencies

Figure 3: Framework of the iterative search procedure for sizing of the grid-forming BESS.

4.1. Searching Objective

The objective of the iterative search is to minimize the LCOH, as described by:

$$\min LCOH = \frac{(C_{\text{init}} + C_{\text{O\&M}}^{\text{fixed}} + C_{\text{O\&M}}^{\text{vari}})}{M^{\text{H}_2}}, \quad (25)$$

where C_{init} is the annualized capital cost; $C_{\text{O\&M}}^{\text{fixed}}$ is the fixed annual operation and maintenance (O&M) cost; $C_{\text{O\&M}}^{\text{vari}}$ is the variable annual O&M cost; and M^{H_2} is the annual hydrogen yield.

The annualized capital cost C_{init} is calculated as follows:

$$C_{\text{init}} = \sum_{j \in \Omega_{\text{F}}} CRF(r, T_j^{\text{LCC}}) S_j c_j^{\text{unit}}, \quad \Omega_{\text{F}} = \{\text{WT, PV, EL, BES}\}, \quad (26)$$

$$CRF(r, T_j^{\text{LCC}}) = \frac{r(1+r)^{T_j^{\text{LCC}}}}{(1+r)^{T_j^{\text{LCC}}}-1}, \quad \text{for } j \in \Omega_{\text{F}}, \quad (27)$$

where S_j is the device capacity; c_j^{unit} is the unit cost of device; $CRF(r, T_j^{\text{LCC}})$ is the capital recovery factor; r is the discount rate (set at 8%); and T_j^{LCC} is the lifetime of the facilities.

The fixed annual O&M cost $C_{\text{O\&M}}^{\text{fixed}}$ is assumed to be a fixed proportion of the initial investment, as expressed by:

$$C_{\text{O\&M}}^{\text{fixed}} = \sum_{j \in \Omega_{\text{F}}} \lambda_j^{\text{O\&M}} S_j c_j^{\text{unit}}, \quad (28)$$

where $\lambda_j^{\text{O\&M}}$ represent the fixed proportion.

The variable annual O&M cost $C_{\text{O\&M}}^{\text{vari}}$ comprises the BESS replacement cost $C_{\text{BES}}^{\text{rep}}$, and the benefit of recycling the retired battery $C_{\text{BES}}^{\text{rec}}$, written as:

$$C_{\text{O\&M}}^{\text{vari}} = C_{\text{BES}}^{\text{rep}} - C_{\text{BES}}^{\text{rec}}, \quad (29)$$

$$C_{\text{BES}}^{\text{rep}} = \sum_{k=1}^{K_{\text{BES}}^{\text{rep}}} S_{\text{BES}}^{\text{rep}} c_{\text{BES}}^{\text{rep}} (1+r)^{-k T_{\text{BES}}^{\text{LCC}} / (K_{\text{BES}}^{\text{rep}} + 1)}, \quad (30)$$

$$C_{\text{BES}}^{\text{rec}} = \sum_{k=1}^{K_{\text{BES}}^{\text{rep}}} S_{\text{BES}}^{\text{rep}} c_{\text{BES}}^{\text{rec}} (1+r)^{-k T_{\text{BES}}^{\text{LCC}} / (K_{\text{BES}}^{\text{rep}} + 1)}, \quad (31)$$

where $S_{\text{BES}}^{\text{rep}}$ is the capacity of the retired battery; $c_{\text{BES}}^{\text{rep}}$ and $c_{\text{BES}}^{\text{rec}}$ are the unit cost and revenue of battery replacement and recycling, respectively; and $K_{\text{BES}}^{\text{rep}}$ is the number of battery replacements.

The number of battery replacements $K_{\text{BES}}^{\text{rep}}$ due to degradation is estimated according to:

$$K_{\text{BES}}^{\text{rep}} = \lceil T_{\text{BES}}^{\text{LCC}} T_{\text{BES}}^{\text{Fail}} - 1 \rceil, \quad (32)$$

$$T_{\text{BES}}^{\text{Fail}} = \Delta E_{\text{BES}}^{\text{degra, max}} / \Delta E_{\text{BES}}^{\text{degra, year}}, \quad (33)$$

where $\lceil \cdot \rceil$ is the ceiling function; $\Delta E_{\text{BES}}^{\text{degra, year}}$ is the annual battery degradation, which is estimated based on the methods in [53, 54] from the simulation data obtained by the high-fidelity model presented in Section 2.3; and $\Delta E_{\text{BES}}^{\text{degra, max}}$ is the maximum allowable degradation and is typically 20%.

The annual hydrogen yield is calculated as:

$$M^{\text{H}_2} = \sum_{t=0}^{8760/\Delta t_{\text{sim}}} \sum_i (\alpha_{\text{P}_2\text{H}}(q_t^{\text{H}_2}) P_{i,t}^{\text{EL}}) \Delta t_{\text{sim}}, \quad (34)$$

Table 3: BESS size preset table for iterative searching

Preset of the BESS size (battery capacity, charging/discharging rate)						
Iterative variable	$S_{\text{BES}}^{\text{ds},0}$	$S_{\text{BES}}^{\text{ds},1}$	$S_{\text{BES}}^{\text{ds},2}$...	$S_{\text{BES}}^{\text{ds},iter-1}$	$S_{\text{BES}}^{\text{ds},iter}$
Size	$(S_{\text{BES}}^{\text{init}}, 2C)$	$(S_{\text{BES}}^{\text{init}} - \Delta S^{\text{BES}}, 2C)$	$(S_{\text{BES}}^{\text{init}} - \Delta S^{\text{BES}}, 3C)$...	$(S_{\text{BES}}^{\text{init}} - \lceil \frac{iter}{2} \rceil \Delta S^{\text{BES}}, 2C)$	$(S_{\text{BES}}^{\text{init}} - \lceil \frac{iter}{2} \rceil \Delta S^{\text{BES}}, 3C)$

$iter \in \mathbb{N}$; ΔS^{BES} is the incremental step; $\lceil \cdot \rceil$ is the ceiling function.

where $\alpha_{\text{P2H}}(q_t^{\text{H}_2})$ is the conversion efficiency function obtained using a 5 MW-rated AEL produced by *Peric Hydrogen Technologies*; see Appendix A.

4.2. Feasibility Testing Constraints

The requirements listed in Section 2.2 serve as constraints in the search for the optimal BESS size. They include grid-forming ability, continuous operation during emergencies, and long-term energy balance. The primary goal of setting these constraints is to ensure frequency and voltage stability and maintain energy balance across timescales. However, these constraints involve multi-timescale transient processes (detailedly discussed in Section 3.5) and the complex interactions among WTs, PV, ELs, and BESS, making explicit quantification challenging. To address this issue, we use refined and simplified electromagnetic transient simulation models presented in Section 2.3 and conduct high-fidelity time-domain simulations to test whether these constraints are satisfied; the detailed procedure is given in Section 4.3.

The frequency and voltage at PCC are key indicators of the OReP2HS stability [55, 56]. Any imbalance in the power and energy in the OReP2HS will finally lead to frequency or voltage changes. Therefore, these indicators serve as criteria for testing all of the constraints:

$$\begin{cases} f_{\min}^{\text{PCC}} \leq f_{\Delta t_{\text{sim}}}^{\text{PCC}} \leq f_{\max}^{\text{PCC}}, \\ V_{\min}^{\text{PCC}} \leq V_{\Delta t_{\text{sim}}}^{\text{PCC}} \leq V_{\max}^{\text{PCC}}, \end{cases} \quad (35)$$

where f_{\min}^{PCC} and f_{\max}^{PCC} are the minimum and maximum frequency limits, respectively; and V_{\min}^{PCC} and V_{\max}^{PCC} are the bus voltage limits; and $f_{t_{\text{sim}}}^{\text{PCC}}$ and $V_{t_{\text{sim}}}^{\text{PCC}}$ represent the frequency and voltage at each time step of the electromagnetic transient simulation.

4.3. Procedure for Searching for the Optimal BESS Size

The optimal BESS size in the OReP2HS is evaluated by a high-fidelity-simulation-based iterative search, as illustrated in Fig. 3.

The process begins by setting an initial BESS size, which includes two key parameters: battery capacity and charging/discharging rate. Then, the iterative search begins. Three subroutines sequentially simulate and test the constraints of grid-forming ability, continuous operation during emergencies, and long-term

energy balance. If any subroutine fails the test, the battery capacity is corrected according to the preset table (shown in Table 3), and the subroutine is re-executed until it passes the test.

The features of each subroutine are designed to address the specific aspects of the BESS sizing process, using different simulation models presented in Section 2.3. The grid-forming ability test simulates the daily operation of the OReP2HS using the proposed EMS and a refined model that accounts for the switching dynamics of the converters and the transient behaviors of PV, WTs, BESS, and ELs. The simulation employs a time step $\Delta t_{\text{sim_GF}}$ of ten microseconds to capture these dynamics accurately. The energy balance test uses the simplified model that considers the transient behaviors of PV, WTs, BESS, and ELs but omits the switching dynamics of the converters. It performs a production simulation over a reference year with a time step $\Delta t_{\text{sim_EB}}$ of one hundred microseconds. The simulation is parallelized over multiple CPUs to speed up the computation. The CODE test evaluates the maximal $N-1$ fault scenarios for both the source and load of the OReP2HS using the refined model. The simulation time step $\Delta t_{\text{sim_N-1}}$ for this test is the same as $\Delta t_{\text{sim_GF}}$. Detailed flowcharts of each subroutine are presented in Fig. 3.

Once all subroutines successfully meet the constraints, we record the feasible BESS sizes. The LCOH for each feasible size is then calculated using (25)–(34). The optimal BESS with the lowest LCOH size is then selected.

5. Results and Discussions

The case study focuses on the OReP2HS planned in Inner Mongolia, China, as described in Section 2.1. The simulation models, detailed in Section 2.3, are developed in *Matlab/Simulink*. The size of the grid-forming BESS and LCOH are evaluated using the search procedure established in Section 4.

The techno-economic parameters and base-case settings are presented in Tables 4 and 5. Fig. 4 shows the meteorological data and on-site forecasts used in the simulations. Local ambient temperature, which affects the PV plant output, is obtained from the *POWER Data Access Viewer* [57] with a time resolution of 1 h. Observed and forecasted wind speeds and solar irradiance data with resolutions of 1 s and 60 s, respectively, are sourced from Lingxiang Wind Farm and Jin’ao PV Plant in Inner Mongolia. The 1-s resolution data are utilized to test grid-forming ability and ensure continuous operation during emergencies, while the 60-s resolution data are used for the annual energy balance test.

5.1. Base-Case Simulation and Evaluation LCOH Results

5.1.1. Production Simulation and BESS Sizing

The optimal size of the grid-forming BESS is evaluated using the iterative search procedure described in Section 4 based on the proposed multi-timescale EMS shown in Fig. 2. The sizing results and corresponding LCOH values are summarized in Table 6, indicating that the optimal BESS size is 6.8 MW/3.4 MWh. The

Table 4: Techno-economic parameters for LCOH evaluation

Facilities	Number	Rating	Investment cost	O&M parameter $\lambda_j^{\text{O\&M}}$	Lifetime of facilities
WT	3	6,250 kW	5,000 CNY/kW		
PV	1	5,000 kW	4,000 CNY/kW		
AEL	4	5,000 kW	3,500 CNY/kW	2 %	20 years
BESS	1	To be evaluated	1,500 CNY/kWh		
Transmission lines	22 km	35 kV	250,000 CNY/km		

Table 5: Base-case parameter settings for production simulation and BESS size search

Parameter	Value	Parameter	Value
T_{RS}	4 h	K_{SOC}	0.0142
$C_{\text{up,h}}^{\text{EL}}$	2 CNY	β	0.286
$C_{\text{up,c}}^{\text{EL}}$	10 CNY	c_j^{rep}	900 CNY/kWh
$C_{\text{down}}^{\text{EL}}$	5 CNY	c_j^{rec}	150 CNY/kWh
s	1,000 CNY/MW	$f_{\text{min}}^{\text{PCC}}$	46.5 Hz
$T_{\text{min}}^{\text{down}}$	1 h	$f_{\text{max}}^{\text{PCC}}$	53.5 Hz
$k_i^{\text{H}_2}$	55.62 kWh/kg	$V_{\text{min}}^{\text{PCC}}$	31.5 kV
$\text{SOC}_{\text{min}}^{\text{BES}}$	10 %	$V_{\text{max}}^{\text{PCC}}$	38.5 kV
$\text{SOC}_{\text{max}}^{\text{BES}}$	90 %	ΔS^{BES}	0.1 MWh
$\Delta t_{\text{sim_EB}}$	5×10^{-4} s	Δt_{RS}	5 min
$\Delta t_{\text{sim_GF}}$	4×10^{-5} s	Δt_{LF}	5 s
$\Delta t_{\text{sim_N-1}}$	4×10^{-5} s	Ramping limit of the EL	0.05 MW/s

battery capacity of the BESS is equivalent to only 13.6% of the maximal hourly total energy output of the WTs and PV plant. The annual costs, including the annualized capital cost and annual O&M cost of the BESS, account for 17.83% of the total annual cost, as illustrated in Fig. 5.

Fig. 6 displays the production simulation results over a reference year, with detailed results from October 1st to October 7th. This period illustrates various operating conditions, including complementary operation, simultaneous fluctuations, and outages of the WT and PV outputs.

First, we discuss the performance of the proposed EMS. With the RS and LF strategies, the electrolytic load tracks the fluctuations in renewable power, optimizing the use of renewable energy and minimizing

Table 6: Base-case result of BESS sizing and LCOH evaluation

Battery size	Charging/Discharging rate	Yearly degradation	LCOH (CNY/kg)
3.4 MWh	2C	4.87 %	33.212

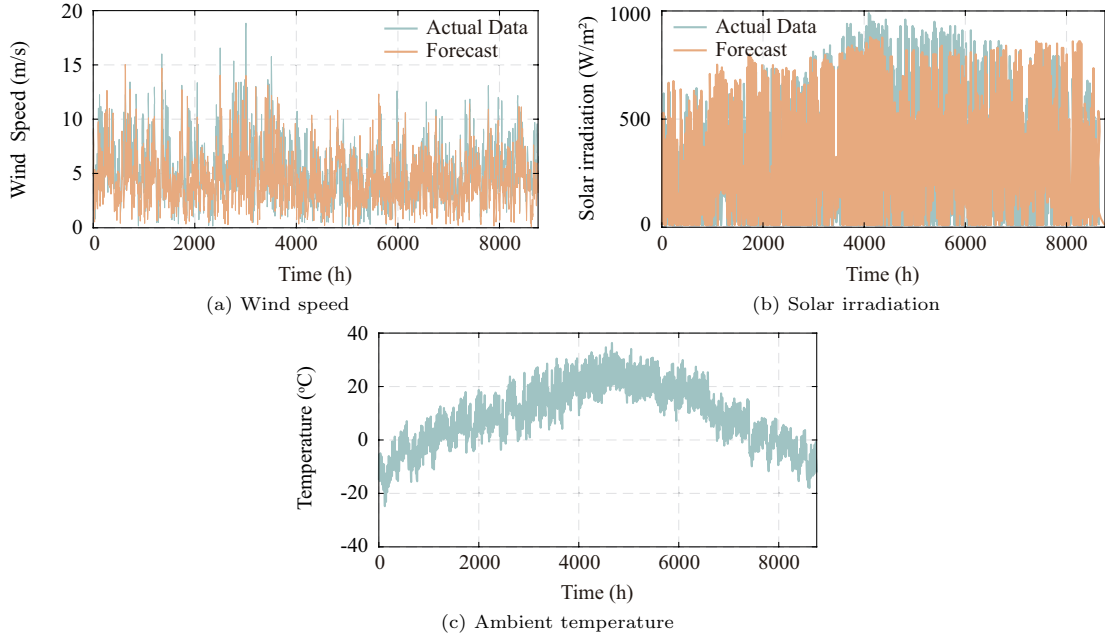


Figure 4: Meteorological data collected from the site of the planned OReP2HS in the case study.

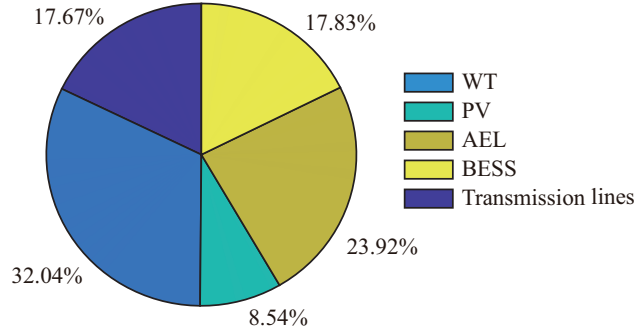


Figure 5: Proportion of investment and annual O&M cost of facilities in the OReP2HS under the optimal BESS size.

the required BESS capacity. For instance, during hours 6,596 to 6,606, only WTs are operational, and the ELs successfully follow wind power fluctuations. However, during hours 6,608 to 6,619, the AELs struggle to match the rapidly changing PV power due to its fast ramping. In these instances, the BESS provides necessary transient power support to maintain power balance under the grid-forming control.

Further analysis of the BESS SOC and power is shown in Fig. 7. The BESS power fluctuates rapidly to smooth out high-frequency renewable power variations. Notably, the active power experiences more frequent fluctuations than the reactive power, emphasizing the need for maintaining frequency stability for the OReP2HS. The SOC of the BESS remains within the allowable range (between 10% and 90%), demonstrating the effectiveness of the SOC correction strategy. The SOC variation resembles that of renewable power, suggesting a temporal correlation between them, which is discussed in detail in Section 5.1.3.

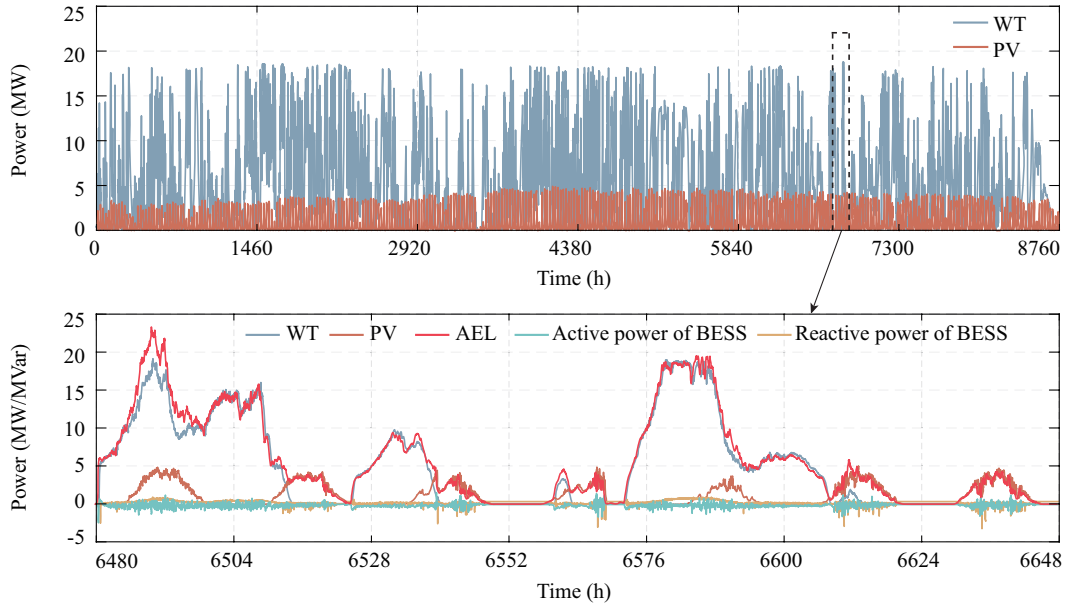


Figure 6: Power of PV, WTs, BESS and AELs in the year-long production simulation.

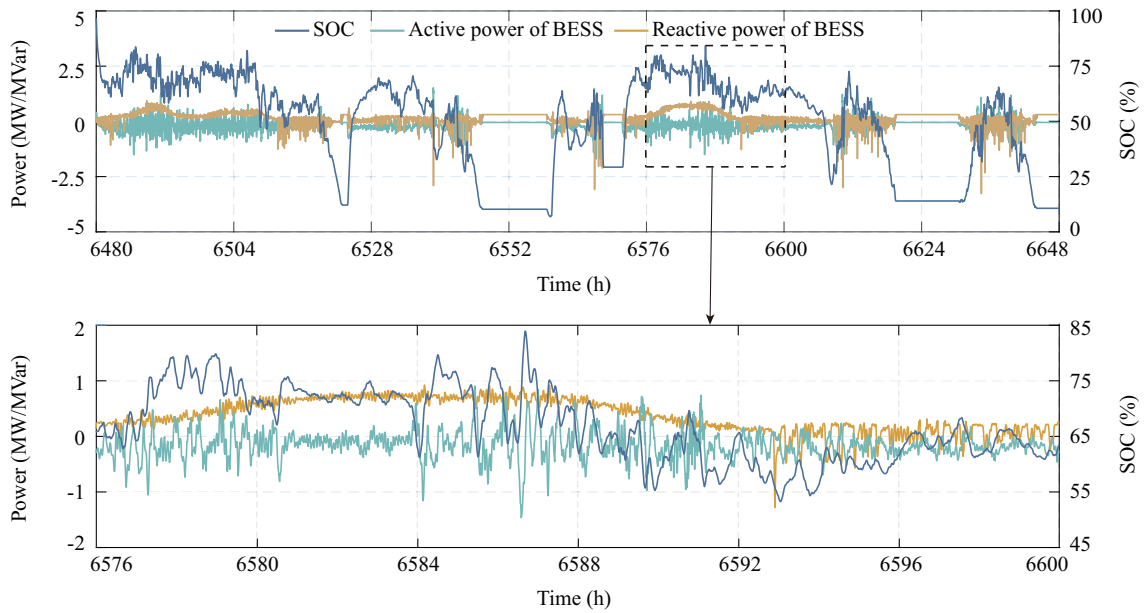


Figure 7: The SOC and active/reactive power of the grid-forming BESS in the year-long production simulation.

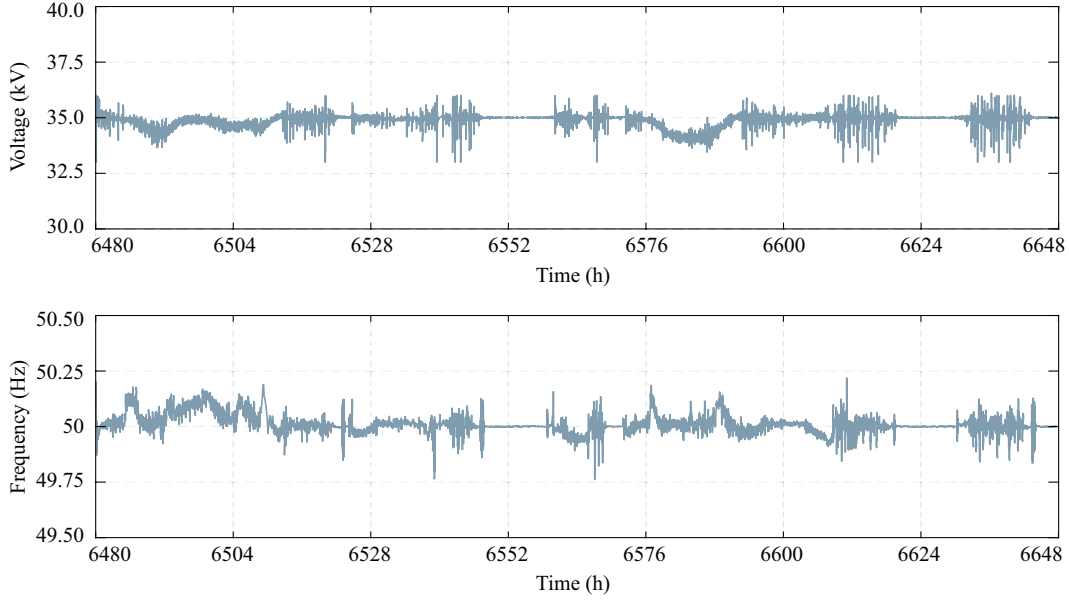


Figure 8: Frequency and voltage at PCC from October 1st to 7th in the production simulation.

Table 7: Technical indexes of the frequency and voltage at PCC

Index	Rated value	Allowable interval	Peak	Nadir	Average	Ratio of the maximal deviation to the rating
Frequency	50 Hz	(46.5 Hz, 53.5 Hz)	50.22 Hz	49.77 Hz	50.02 Hz	0.46%
Voltage	35 kV	(31.5 kV, 38.5 kV)	36.00 kV	33.01 kV	34.89 kV	5.69%

Finally, the frequency and voltage at the PCC from October 1st to 7th are presented in Fig. 8. These variations are consistent with the active and reactive power of the BESS shown in Fig. 7, respectively. Table 7 confirms that the frequency and voltage stay within acceptable limits throughout the period, validating the effectiveness of the EMS in maintaining stability.

5.1.2. Operation During Emergencies

In this section, we conduct a WT tripping test to analyze the performance of the proposed EH strategy. The BESS size is set at 6.8 MW/3.4 MWh as obtained in Section 5.1.1, and the following settings are compared:

Setting A: The EH is automatically activated based on its activation criteria listed in Table 2, as in the proposed EMS used in search for the optimal BESS size in Section 5.1.1.

Setting B: The EH is removed, and other sub-strategies of the EMS remain consistent with Setting A.

The simulation results with a WT tripping at 5 s are depicted in Figs. 9 and 10. When the WT trips at 5 s, the frequency drops sharply, while the BESS output increases rapidly to prevent frequency collapse. The EH is activated when the frequency deviation reaches 0.35 Hz. Subsequently, power shedding commands are

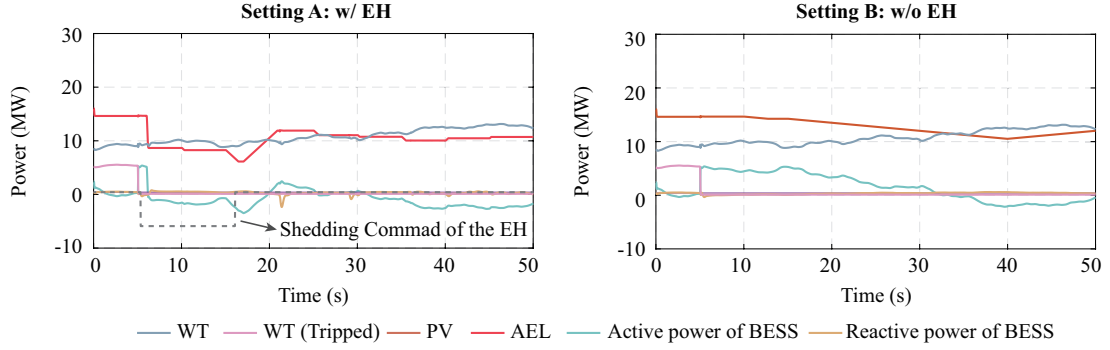


Figure 9: The power variations of PV, WTs, BESS and AELs when a WT is tripped.

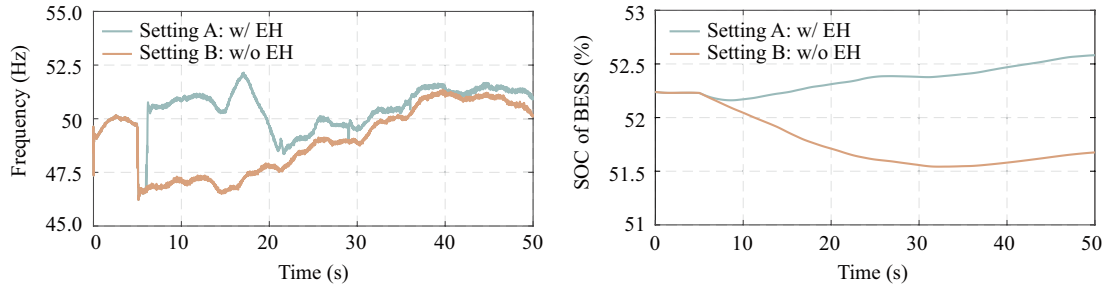


Figure 10: The frequency and SOC variation when a WT tripped.

sent to all AELs. The electrolytic load decreases from 15 MW to 10 MW with a maximal ramping rate of 0.5 MW/s after 1 s, allowing the frequency to recover to its rated value within 1.5 s. Meanwhile, the BESS output decreases back to the initial state.

By contrast, without the EH, AELs cannot be regulated to respond promptly to the power loss. Their loads slowly reduce from 15 MW to 10 MW as commanded by the LF strategy. This process takes nearly 29 s, causing the frequency to increase tardily. During this period, the BESS maintains its output to balance the power loss, leading to a decrease of 0.8% in its SOC.

Note that the system remains stable when the WT is tripped in both settings (w/ and w/o enabling the EH strategy). The proposed EH utilizes the flexibility of AELs to mitigate SOC variation during emergencies, thereby reducing the required BESS capacity. We also want to remark that although the proposed EH is reasonably effective, further exploration is needed to fully understand the potential and limitations of OReP2HS in addressing emergencies.

5.1.3. Correlation Between the SOC and Renewable Outputs

As observed in Fig. 7, the SOC of the BESS tends to resemble the fluctuations in the renewable power outputs. To explore potential strategies for reducing the BESS size, we investigate the relationship between renewable power and the grid-forming BESS under the proposed EMS.

Fig. 11 illustrates the local extrema in SOC and renewable power for March. Whenever renewable power

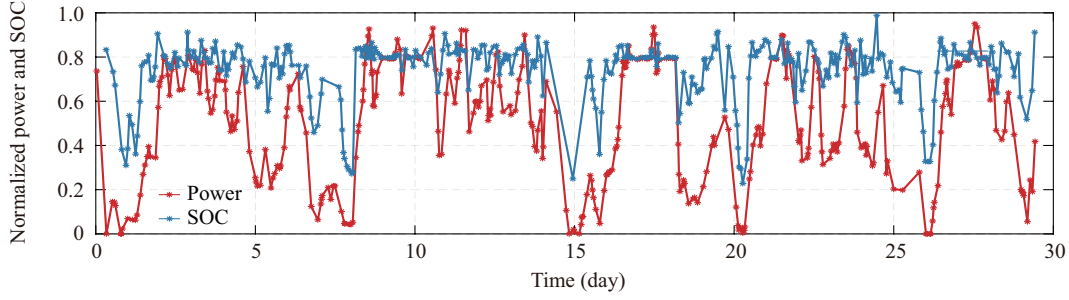


Figure 11: Temporal variations of local extrema in the SOC of the BESS and renewable output in March.

Table 8: Rank correlation between the SOC of BESS and renewable power in each month

	Mar.	Apr.	May	Jun.	Jul.	Aug.	Sep.	Oct.	Nov.	Dec.	Jan.	Feb.
Rank correlation	0.855	0.851	0.871	0.902	0.870	0.835	0.833	0.858	0.845	0.896	0.858	0.847

reaches a local extremum, a corresponding peak in SOC occurs shortly afterward, indicating a temporal correlation between their fluctuations.

A statistical analysis of the yearly SOC and renewable power output with 1-min resolution is presented in Fig. 12. As shown in Fig. 12a, the SOC exhibits a positive and nonlinear relationship with renewable power. The SOC changes rapidly in the lower renewable output range (normalized power ranging from 0 to 0.4). During this interval, the precision of fast forecasting integrated into the LF strategy influences the outputs and SOC of the BESS. Frequent and irregular ramps of the renewable power complicate accurate forecasting, necessitating frequent BESS output adjustments, as shown in the local statistics in Fig. 12b. This phenomenon leads to an almost linear relationship between SOC and renewable power in this range.

By contrast, when renewable generation operates at a higher output interval (normalized power from 0.4 to 1), the outputs are relatively stable. During these periods, AELs consume nearly all renewable outputs, leaving the BESS to balance minor power fluctuations, and causing the SOC of the BESS to become less correlated with renewable power.

Additionally, Fig. 12b shows that the normalized SOC distribution is mainly concentrated around 0.15 and 0.75, indicating that the BESS frequently operates in deep charge or discharge states. Consequently, the BESS experiences a rapid degradation rate of 4.87% annually.

Table 8 quantifies the positive correlation between SOC and renewable power. This correlation suggests that SOC prediction based on renewable power forecasts can enable actions to mitigate battery degradation, optimize BESS energy management, and potentially further reduce the BESS size.

5.2. Comparison of the Optimal BESS Size with Different EMS Under Stability Constraints

As summarized in Section 1.2, existing EMSs supporting the design of OReP2HS are predominantly based on rule-based or optimization-based approaches with time resolutions ranging from at least 5 min

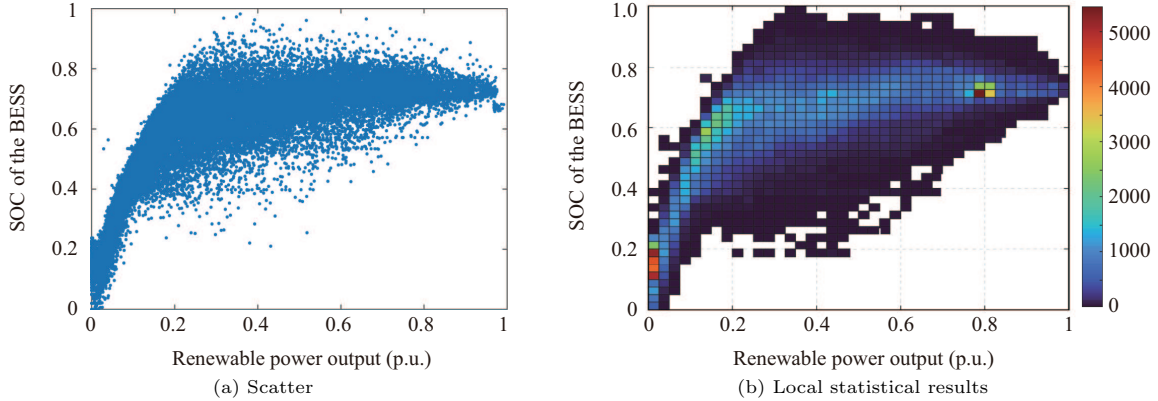


Figure 12: Statistical relationship between the SOC of the BESS and renewable power.

to 1 h. The components of the OReP2HS are optimized based on these EMSs considering only the power balance of PV, WTs, AELs, and BESS at discrete time steps, without accounting for the transient power balance requirements that are essential for maintaining voltage and frequency stability.

However, an OReP2HS must coordinate PV, WTs, AELs, and BESS to maintain power balance on the transient time scale (milliseconds to seconds) to ensure voltage and frequency stability. The EMSs reported in the literature and summarized in Section 1.2 ensure the power balance of PV, WTs, AELs, and BESS at discrete time points in scheduling (every 5 minutes or hourly), but they cannot maintain power balance on the transient timescale. In particular, BESS may overcharge or over-discharge between these discrete points, losing its grid-forming ability and causing instability. Therefore, the design of OReP2HS based on EMS with 5-min or 1-h resolutions may lead to the underestimation of the BESS size required to ensure the stability of OReP2HS.

Therefore, we compared the optimal BESS sizes obtained under the proposed EMS and under the EMSs reported in the literature [30, 38, 40, 41] with 5-minute time resolution while considering system transient power balance constraints. The optimal BESS size for each case is evaluated using the high-fidelity simulation-based search procedure (as shown in Fig. 2, which considers the voltage and frequency stability constraints). Then, we use the optimal configuration ratio ρ^{Bat} of battery capacity (defined as the ratio of the battery size to the rated hourly energy output of power sources, as $\rho^{\text{Bat}} = S^{\text{Bat}} / (S^{\text{PV}} + \sum_{i=1}^m S_i^{\text{WT}})$) to quantify the influence of the stability constraints on the optimal battery size. The results are listed in Table 9.

Benchmark 1: A rule-based EMS from [40, 41]. The strategy is as follows: if the renewable power exceeds the minimal load of AELs, the AELs are started up, and then the electrolytic load tracks the renewable power with a time step of 5 min. When the maximal loads of AELs are reached, the rest of the power charges the BESS. When the combined power from PV, WTs, and the BESS is insufficient to keep the AELs at their minimum load, the AELs are shut down.

Table 9: Optimal BESS size and LCOH under different EMS considering stability constraints

EMS	The optimal battery capacity ρ^{Bat}		Charging/ Discharging rate	Yearly battery degradation	LCOH (CNY/kg)
	Reported in literature (Do not consider stability constraints)	Evaluated in this paper considering stability constraints			
Benchmark 1	3.6% [40]	69.44% (17.36 MWh)	1C	3.91%	56.958
Benchmark 2	26.28%~40.11% [38]	55.67% (13.94 MWh)	1C	3.55 %	51.737
The proposed	/	13.6% (3.4 MWh)	2C	4.87 %	33.212

Benchmark 2: An MILP-based EMS similar to those in [30, 38]. AELs and the BESS track the renewable power only based on an MILP-based scheduling. For fair comparison, we take (1)–(17) introduced in Section 3.2 as the MILP model and set the time step as 5 min.

An examination of the data presented in Table 9 shows that the values of the optimal configuration ratio of battery capacity evaluated in the literature [38, 40], which neglects the voltage and frequency constraints, are significantly lower than those evaluated in our study which are obtained considering voltage and frequency constraints. This indicates that battery capacity is underestimated in the previous studies. Underestimation of the battery capacity may make it difficult for an OReP2HS to maintain stable operation and may lead to an overly optimistic assessment of LCOH.

Furthermore, when considering voltage and frequency stability constraints in the design of OReP2HS, the battery capacity and LCOH evaluated in benchmarks 1 and 2 (with only a rule-based and an optimization-based EMS) are higher than those assessed based on our proposed EMS. This result demonstrates that the proposed EMS achieves more effective and efficient energy utilization across timescales, ultimately leading to a lower requirement for the size of the BESS and lower-cost hydrogen production.

5.3. Sensitivity Analysis

Taking advantage of the load flexibility of AELs, part of the energy balance regulation requirements for the grid-forming BESS is replaced, thus reducing the BESS size and LCOH. The load flexibility of AELs is significantly influenced by two key parameters in the EMS: the time step of the LF, Δt_{LF} , and the load ramping limit of AELs. Therefore, a sensitivity analysis of these two parameters is performed to provide a comprehensive understanding of the limitations of the proposed EMS and to explore the potential for further reducing the BESS size and LCOH.

For the sensitivity analysis, six parameter setting groups are considered for comparison. In each group, the ramping limit of AELs is kept constant while the time step of the LF is increased stepwise. The results of the sensitivity analysis are listed in Table 10.

Table 10: Sensitivity analysis result of the optimal BESS size and LCOH with different parameter settings

Parameter setting	Time step of LF Δt_{LF}	Ramp limit of AEL (MW/s)	Optimal battery size (MWh)/ Charging and discharging rate	Yearly degradation of battery	LCOH (CNY/kg)
Base	5 s	0.05	3.40/2C	4.87%	33.212
I	10 s	0.05	3.75/2C	4.88%	33.767
	15 s	0.05	4.04/2C	4.91%	34.281
	30 s	0.05	4.62/2C	5.01%	38.063
	60 s	0.05	5.07/2C	4.97%	39.951
	90 s	0.05	5.73/2C	4.99%	42.211
II	5 s	0.1	3.05/2C	4.94%	31.551
	10 s	0.1	3.18/2C	4.94%	32.777
	15 s	0.1	3.56/2C	5.04%	33.437
	30 s	0.1	3.96/2C	5.04%	35.133
	60 s	0.1	4.14/2C	5.05%	35.891
	90 s	0.1	4.87/2C	5.12%	38.715
III	5 s	0.2	2.78/2C	4.94%	31.018
	10 s	0.2	2.89/2C	4.93%	31.275
	15 s	0.2	3.24/2C	5.03%	32.881
	30 s	0.2	3.60/2C	5.11%	33.507
	60 s	0.2	3.76/2C	5.12%	34.785
	90 s	0.2	4.32/2C	5.14%	36.559
IV	5 s	0.3	2.66/2C	4.92%	30.872
	10 s	0.3	2.80/2C	4.97%	31.116
	15 s	0.3	3.14/2C	5.05%	32.707
	30 s	0.3	3.49/2C	5.13%	33.316
	60 s	0.3	3.64/2C	5.14%	33.977
	90 s	0.3	4.15/2C	5.14%	35.463
V	5 s	0.4	2.66/2C	4.97%	30.799
	10 s	0.4	2.80/2C	4.97%	31.115
	15 s	0.4	3.10/2C	5.10%	32.634
	30 s	0.4	3.43/2C	5.11%	33.211
	60 s	0.4	3.59/2C	5.15%	33.699
	90 s	0.4	4.07/2C	5.16%	35.324
VI	5 s	0.5	2.66/2C	4.97%	30.799
	10 s	0.5	2.80/2C	4.97%	31.109
	15 s	0.5	3.08/2C	5.10%	32.602
	30 s	0.5	3.39/2C	5.11%	33.142
	60 s	0.5	3.56/2C	5.15%	33.437
	90 s	0.5	4.02/2C	5.16%	35.237

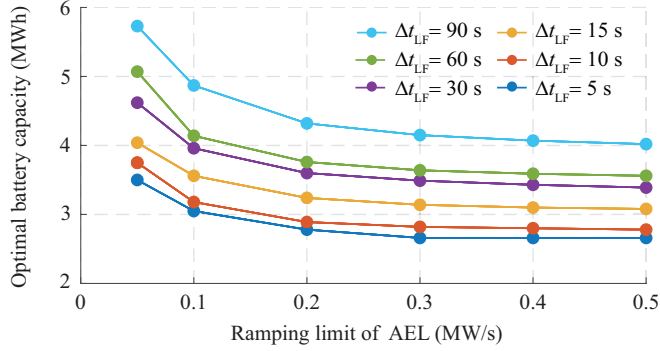


Figure 13: Optimal battery capacities with respect to different time steps of the LF and the ramping limit of the AEL.

5.3.1. Optimal BESS Size with Different Parameter Settings

Figs. 13 and 14 show the results of the sensitivity analysis. The results indicate that the optimal battery capacity increases almost exponentially when the ramping limit of AELs is lower than 0.3 MW/s (6% of the rated power) across all configurations. When the ramping limit exceeds 0.3 MW/s, the battery capacity decreases slightly by 2%, indicating that the ramping limit of 0.3 MW/s for AELs is a critical inflection point for battery capacity optimization.

Additionally, the reduction in the optimal battery capacity due to a decrease in the LF time step is more significant than that caused by an increase in the ramping limit. Numerically, as the time step and ramping limit increase to ten times their base values, the average reductions in the battery capacities are 0.876 MWh and 0.484 MWh, respectively. This demonstrates that the time step has a more substantial impact on sizing of the BESS. Therefore, with the proposed multi-timescale EMS, a shorter time step for the LF has a more pronounced effect than a higher load ramping limit of AELs. Meanwhile, under optimal sizing, the yearly degradation of the battery remains relatively constant at approximately 5%, indicating that the BESS is fully utilized by the proposed EMS across different parameter settings.

An examination of Fig. 14 shows that the minimal battery capacity of 2.66 MWh is obtained when the ramping limit of AELs reaches 0.5 MW/s with a 5-s time step for the LF. However, it may be challenging to design the ramping at 0.5 MW/s (10% of the rated power) for utility-scale AELs [58]. Setting the ramping limit in the range of 0.2 MW/s to 0.3 MW/s with a 5-s or 10-s time step for a 5 MW-rated AEL in the LF is more advisable based on our experiments on several 5 MW-rated commercial AELs, and the BESS size remains in an acceptable range of between 2.66 and 2.89 MWh.

5.3.2. LCOH with Different Parameter Settings

This section discusses the impact of various factors on the LCOH, with the results shown in Fig. 15. It is observed that the cost of hydrogen decreases almost linearly with the decreasing time step of LF. Moreover, the rate of change of LCOH is significantly higher when the time step is shorter than 30 s. The ramping

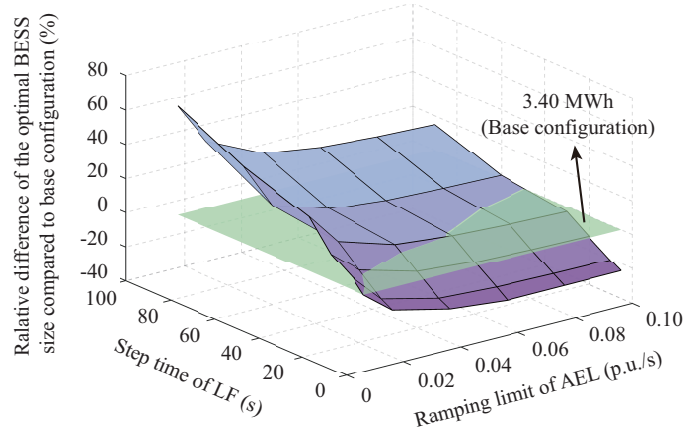


Figure 14: The ratio of the optimal battery capacities between the base parameter setting and other settings.

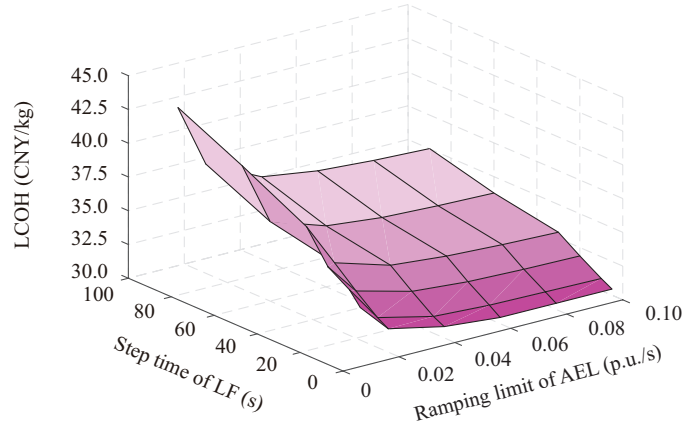


Figure 15: LCOH with respect to different time steps of the LF and ramping limit of the AEL.

limit of AELs has a minimal impact on LCOH after it exceeds 0.3 MW/s. However, when the ramping limit drops below 0.3 MW/s, the LCOH rises exponentially, reaching its maximum value at 0.05 MW/s in all evaluated configurations.

Comparison with Fig. 15 shows that the trend for the LCOH, which is influenced by both the ramping limit and the time step of LF, is similar to that of BESS size. This similarity indicates that the annual costs, including the capital cost and O&M cost of BESS, significantly affect the LCOH. The minimal LCOH of 25.451 CNY/kg (3.510 USD/kg) appears when the ramping limit of AELs is 0.5 MW/s with a 5-s time step for the LF. When the ramping limit is set within the recommended range of 0.2 MW/s to 0.3 MW/s with a 5-s or 10-s time step for the LF, the LCOH also remains competitive, ranging from 25.458 CNY/kg (approx. 3.511 USD/kg) to 26.246 CNY/kg (approx. 3.620 USD/kg).

6. Conclusions and Outlook

6.1. Conclusions

To maintain stability while ensuring the economic profitability of the OReP2HS, this work presents a multi-timescale EMS that coordinates the energy balance from transient power balance to intra-day scheduling for PV, WTs, grid-forming BESS, and AELs. The optimal BESS size under the proposed EMS is evaluated using a high-fidelity simulation-based search procedure, considering constraints related to the grid-forming capability, continuous operation during emergencies, and long-term energy balance that cover timescales ranging from milliseconds to a year.

A realistic OReP2HS planned in Inner Mongolia, China, is used as a case study. The studied system includes 18.75 MW WTs, a 6.25 MWp PV plant, and four AELs, each rated at 5 MW. The optimal size of the grid-forming BESS is evaluated to be 6.8 MW/3.4 MWh, with the battery capacity accounting for 13.6% of the rated hourly energy output of the renewable power sources. However, the BESS exhibits a significant annual degradation rate of 4.87%, increasing its O&M costs for replacing retired batteries. Consequently, the capital expenditures of the BESS account for 17.83% of the total, and the minimal LCOH under the base-case setting is evaluated to be 33.212 CNY/kg (4.581 USD/kg).

We also find that without considering voltage and frequency stability, the BESS size would be underestimated by approximately 15–30% by the methods used in the studies reported in the literature, indicating that stability constraints are necessary in the design of the OReP2HS. Additionally, the SOC of the BESS shows a positive correlation with renewable power. This implies that SOC can be predicted based on renewable power forecasts, enabling predictive measures to mitigate battery degradation.

Finally, sensitivity analysis shows that the required BESS size decreases when increasing the load ramping rate of AELs or shortening the time step of the LF control. Reducing the adjustment time step of the electrolytic load from 90 to 5 s and increasing its load ramping limit from 1% to 10% of the rated electrolytic load reduces the BESS size from 5.73 MWh to 2.66 MWh and the LCOH from 37.814 CNY/kg (approx. 5.216 USD/kg) to 25.458 CNY/kg (approx. 3.511 USD/kg). Considering the cost for the design, manufacture, and maintenance of utility-scale AELs with fast load regulation capability, an electrolytic load ramping limit at 4–6% of the rated power and an adjustment time step at 5 or 10 s are recommended for the AEL to balance profitability and technological feasibility.

6.2. Outlook

Even though this work proposes a multi-timescale EMS and investigates the optimal size of the grid-forming BESS required for an OReP2HS, several future research directions need to be explored.

First, as mentioned in Section 3, the proposed EMS requires further refinement. Future work should include the consideration of the probabilistic characteristics of renewable power, refining of rolling scheduling, and integration of pre-actions of BESS control into the EMS to improve the OReP2HS performance.

Second, the iterative searching procedure presented in Section 4 is designed for evaluation of the BESS size. However, for OReP2HS planning, the sizes of the electrolyzers, power sources, and the electrical network also must be determined in some cases, making the dimension of the search space much larger. Given the complicated dynamics of the OReP2HS across timescales, a more efficient and mathematically advanced optimization approach is desired for future research.

Finally, industrial-scale OReP2HSs may be connected to downstream hydrogen buffer tanks, hydrogen delivery and refueling systems, and hydrogen consumers, such as green ammonia and methanol synthesis, melting, or refining. The proposed EMS, particularly for long-term energy balance and intra-day rolling scheduling, needs to be improved to cover these downstream sections; this is another important direction for future research.

Acknowledgement

The authors gratefully acknowledge the financial support from the National Key Research and Development Program of China (2021YFB4000503) and the National Natural Science Foundation of China (52377116, 52377115, and 52307126).

Declaration of Interest

None.

Data Availability

The data related to this work are available upon request.

Appendix A. Details of the Simulation Models

The topologies and parameters of each component in both the refined and simplified simulation models are elaborated below.

Appendix A.1. PV Plant

Fig. A1 depicts the PV plant model. It consists of a boost converter, a three-phase inverter, an AC filter, and a transformer connecting the PV array to the OReP2HS. The standard PV array module in the Simulink/Simscape environment is employed, and we set its parameters to meet the specifications of the PV plant in our studied case. The controllers and parameters of the PV plant model are shown in Table A1.

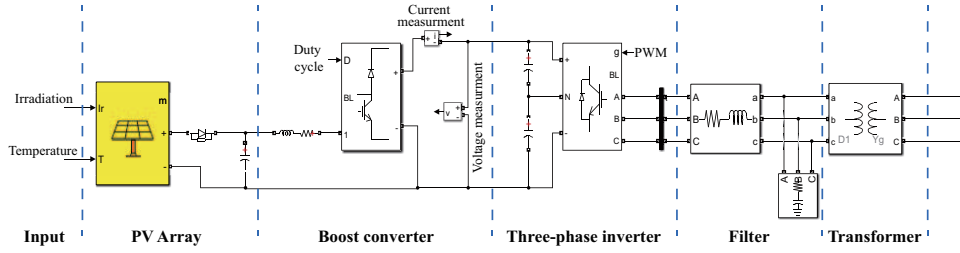


Figure A1: Topology of the PV plant model.

Table A1: Parameters of the PV plant model

Module	Parameter	Value
PV Array	Rated power of the PV array	5.014 MW
	Maximal power of per cell	540.2 W
	Open circuit voltage of per cell	49.5 V
	Short-circuit current of per cell	13.85 A
	Voltage at maximum power point	41.65 V
	Current at maximum power point	12.97 A
	Maximal power of per cell	540.2 W
Boost converter	Controller	MPPT
Three-phase inverter	Rated DC Voltage	1,500 V
	Rated AC voltage	630 V
	Rated frequency	50 Hz
Transformer	Control	DC voltage control
	Rated capacity and frequency	5.0 MVA, 50 Hz
	Primary voltage (RMS)	35 kV
	Secondary voltage (RMS)	630 V

Appendix A.2. Wind Turbine

Fig. A2 depicts the wind turbine model. A DFIG-based wind farm model in the Simulink/Simscape environment is employed, and its parameters are set to meet the specifications of the case study. The controllers and parameters of the wind turbine model are shown in Table A2.

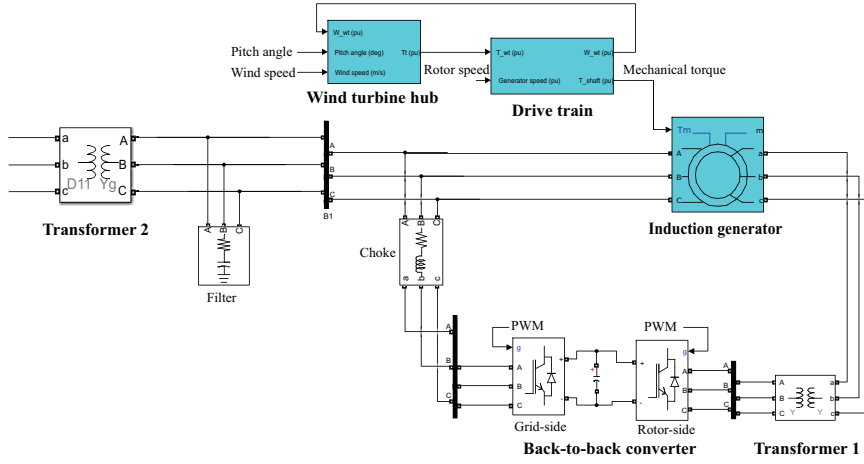


Figure A2: Topology of the wind turbine model.

Table A2: Parameters of the wind turbine model

Module	Parameter	Value
Wind turbine hub	Rated power	6.25 MW
	Impeller diameter	175 m
	Swept area	24,053 m ³
	Rated speed	10.2 m/s
	Cut-in speed	3 m/s
	Cut-off speed	24 m/s
Drive train	Inertia constant	5.25 s
	model	2-mass model
Induction Generator	Rated capacity	6.25 MVA
	Rated voltage	690 V
	Rated frequency	50 Hz
Back-to-back converter	Rated capacity of the grid side	1084 kVA
	Rated capacity of the rotor side	2,174 kVA
	Rated AC voltage	1,140 V
	Grid-side controller	DC voltage control
	Rotor-side controller	P/Q control
Transformer 1	Rated capacity and frequency	6.25 MVA, 50 Hz
	Primary voltage (RMS)	1970 V
	Secondary voltage (RMS)	690 V
Transformer 2	Rated capacity and frequency	6.25 MVA, 50 Hz
	Primary voltage (RMS)	35 kV
	Secondary voltage (RMS)	1140 V

Appendix A.3. BESS

The BESS model is depicted in Fig. A3. It includes a three-phase bi-directional inverter, an AC filter, and a transformer. The battery itself is modeled as a controllable ideal DC source in series with an internal resistance. The controllers and parameters of the BESS are summarized in Table A3.

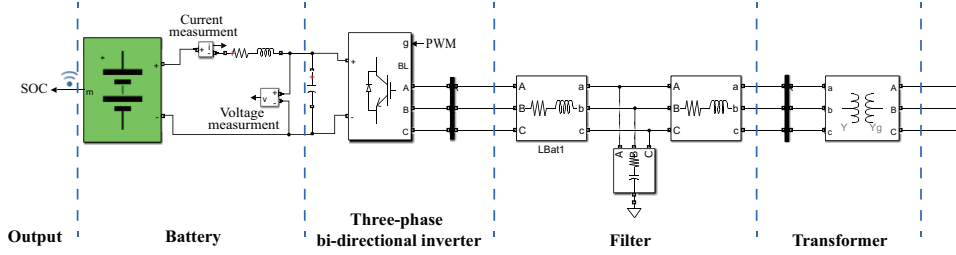


Figure A3: Topology of the BESS model.

Table A3: Parameters of the BESS model

Module	Parameter	Value
Battery	Rated capacity of the battery	3.4 MWh
	Charging/discharging rate	2C
	Rated capacity of per cell	280 Ah
	Rated Voltage of per cell	3.2 V
	Operating voltage of per cell	2.8 V~4.0 V
Three-phase bi-directional inverter	Internal resistance	0.39 M Ω
	Rated DC Voltage	1300 V
	Rated AC voltage	690 V
Transformer	Rated frequency	50 Hz
	Controller	V-F droop control
Transformer	Rated capacity and frequency	3.5 MVA, 50 Hz
	Primary voltage (RMS)	35 kV
	Secondary voltage (RMS)	690 V

Appendix A.4. AEL

The AEL model is depicted in Fig. A4. It includes a stack, a Buck-Boost converter, a three-phase rectifier, an AC filter, and a transformer connecting the AEL to the OReP2HS. The stack is represented by an equivalent circuit consisting of an internal resistance in series with a controllable DC voltage source to simulate its voltage-current (U-I) characteristics, as shown in Fig. A5. The controllers and parameters of the AEL model are summarized in Table A4.

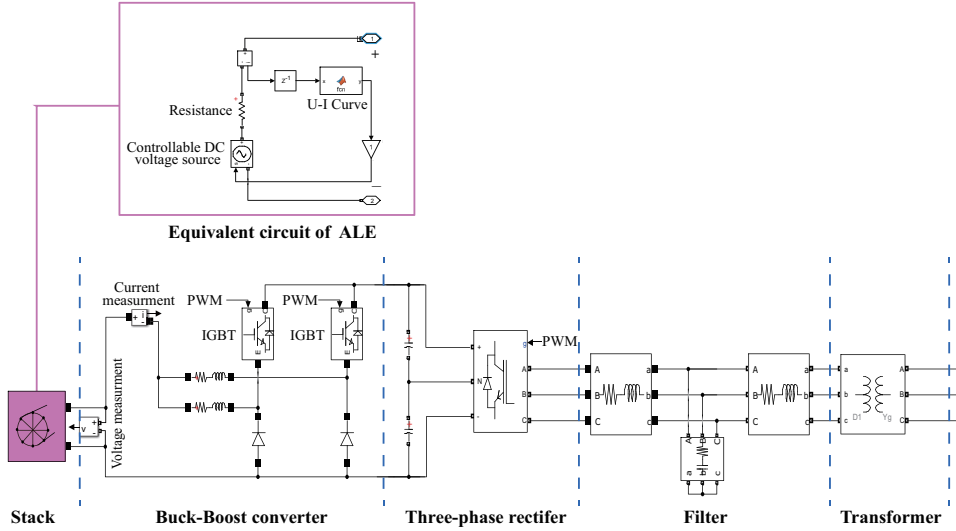


Figure A4: Topology of the AEL model.

Table A4: Parameters of the AEL model

Module	Parameter	Value
Equivalent circuit of AEL	Resistance	0.05 Ω
	U-I curve	Depicted in Fig. A5
Buck-Boost converter	Controller	DC current control
	Rated capacity	5.0 MW
Three-phase inverter	Rated AC voltage	750 V
	Controller	DC voltage control
Transformer	Rated capacity and frequency	6.0 MVA, 50 Hz
	Primary voltage (RMS)	35 kV
	Secondary voltage (RMS)	380 V

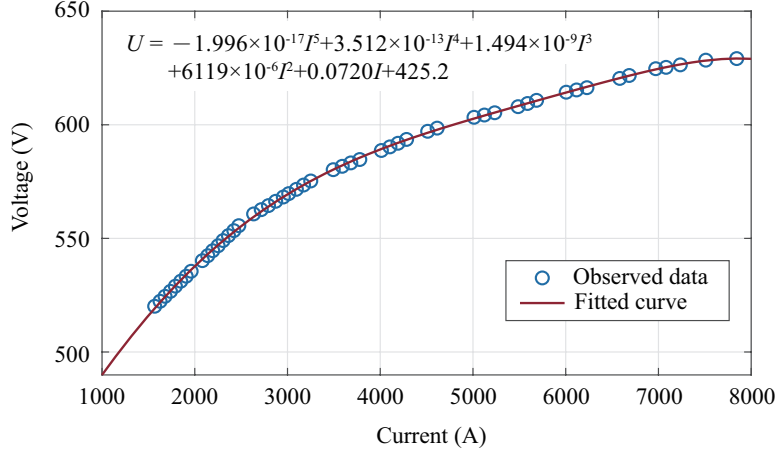


Figure A5: The experimental and fitted U-I curve of a 1,000 Nm³/h-rated electrolysis stack produced by Peric Hydrogen Technologies.

Appendix B. Nomenclature

Abbreviations

AC	Alternating current	Δt_{RS}	Time step of the scheduling
EL	Electrolyzer	Δt_{LF}	Time step of LF control
BESS	Battery energy storage system	$\Delta E_j^{\text{degra,max}}$	Battery degradation limit
EMS	Energy management system	β	Intercept of SOC correction control
LCOH	Levelized cost of hydrogen	$\lambda_j^{\text{O\&M}}$	Ratio of annual O&M cost
MA	Moving average	η^{BES}	BESS Charge/discharge efficiency
MILP	Mixed-integer linear programming	<i>Variables</i>	
MPPT	Maximum power point tracking	C_{init}	Initial investment cost
OReP2HS	Off-grid renewable P2H system	$C_{\text{O\&M}}^{\text{fixed}}$	Fixed annual O&M cost
PCC	Point of common connection	C_j^{rep}	Battery replacement cost
PV	Photovoltaic	C_j^{rec}	Battery recycling revenue
ReP2H	Renewable power to hydrogen	$C_{\text{O\&M}}^{\text{vari}}$	Variable annual O&M cost
RoCoF	Rate of change of frequency	<i>iter</i>	Iterator in battery size search
O&M	Operation and maintenance	M^{H_2}	Annual hydrogen yield
SOC	State of charge of battery	K_j^{rep}	Battery replacement times
LF	Load following	$P_{i,t}^{\text{EL}}$	Load power of AEL
WT	Wind turbine	$P_{\text{sb}}^{\text{EL}}$	Standby power of EL
<i>Parameters</i>		$P_{i,t}^{\text{EL,RS}}$	Baseline load command of EL
$C_{\text{up,h/c}}^{\text{EL}}$	Hot/cold startup costs of EL	$P_{i,t}^{\text{EL,LF}}$	Load correction command of EL

$C_{\text{down}}^{\text{EL}}$	Costs for hot/cold start-up of EL	$P_t^{\text{BES,C/D}}$	BESS Charging/discharging power
C^{H_2}	Selling price of hydrogen	\hat{P}_t^{RES}	Fast prediction in LF control
C_j^{rep}	Unit replacement cost of device j	$\hat{P}_{i,t}^{\text{WT/PV,cut}}$	Power curtailment of WT/PV
C_j^{rec}	Unit recycling revenue of device j	$\hat{P}_{i,t}^{\text{WT/PV}}$	Ultra-short-term forecast of WT/PV
C_j^{unit}	The unit cost of device j	S_j	Capacity of device j
$f_{\text{min/min}}^{\text{PCC}}$	Frequency limits	S_j^{rep}	Replacement capacity of device j
$K_i^{\text{H}_2}$	Energy conversion coefficient of AEL	S_j^{rec}	Recycling capacity of device j
r	Discount rate	$\text{SOC}_t^{\text{BES}}$	State of charge of battery
$S_{\text{init}}^{\text{BES}}$	Initial size of BESS in the search	S_i^{EL}	Capacity of electrolyzer
$\text{SOC}_{\text{min/max}}^{\text{BES}}$	Battery state of charge limits	$S_{\text{BES}}^{\text{ds,iter}}$	Iterator in battery sizing
s	Penalty for power curtailment	T_j^{Fail}	Durable years of device j
T_{RS}	Total time periods of scheduling	$\mu_t^{\text{BES,C/D}}$	BESS Charging/discharging state
$T_{\text{min}}^{\text{down}}$	Minimal restart interval for AEL	$\mu_{i,t}^{\text{st}}/\mu_{i,t}^{\text{sb}}/\mu_{i,t}^{\text{sp}}$	Production/standby/shut-down state of AEL
T_j^{LCC}	Lifetime of device j	$\mu_{i,t}^{\text{up,h}}/\mu_{i,t}^{\text{up,c}}/\mu_{i,t}^{\text{down}}$	Action of hot start-up/cold start-up/shut-down of AEL
$V_{\text{min/max}}^{\text{PCC}}$	Voltage limits	$\Delta E_j^{\text{degra,year}}$	Annual degradation of BESS
$r_{\text{min/max}}^{\text{EL}}$	Load regulation limits of EL		

References

References

- [1] X. Meng, M. Chen, A. Gu, X. Wu, B. Liu, J. Zhou, Z. Mao, China's hydrogen development strategy in the context of double carbon targets, *Natural Gas Industry B* 9 (6) (2022) 521–547.
- [2] Y. Li, H. Phoumin, S. Kimura, Hydrogen sourced from renewables and clean energy: A feasibility study of achieving large-scale demonstration, *Economic Research Institute for ASEAN and East Asia*.
- [3] R. Dufo-López, J. M. Lujano-Rojas, J. L. Bernal-Agustín, Optimisation of size and control strategy in utility-scale green hydrogen production systems, *International Journal of Hydrogen Energy* 50 (2024) 292–309.
- [4] Y. He, Y. Zhou, J. Yuan, Z. Liu, Z. Wang, G. Zhang, Transformation towards a carbon-neutral residential community with hydrogen economy and advanced energy management strategies, *Energy Conversion and Management* 249 (2021) 114834.
- [5] P. Group, Yuri lets construction contract to T.EN for green hydrogen plant in Australia, *PetroChemical News*.
- [6] Invest 24.5 billion yuan! Bidding for the demonstration project of 500000 t / an off-grid landscape hydrogen production and green ammonia synthesis in China Coal Ordos-Polaris Hydrogen Energy Network.
URL <https://m.bjx.com.cn/mnews/20221221/1277700.shtml>
- [7] The first demonstration project of 1000-ton solar power generation, hydrogen production by electrolysis of water, and methanol synthesis from carbon dioxide and hydrogen has been successfully tested, *Coal Chemical Industry* 48 (2020) 1.

- [8] Z. Abidin, C. Webb, E. Gray, Solar hydrogen hybrid energy systems for off-grid electricity supply: A critical review, *Renewable and sustainable energy reviews* 52 (C) (2015) 1791–1808.
- [9] J. He, K. Chen, M. Li, Y. Luo, C. Liang, Y. Xu, Review of protection and fault handling for a flexible DC grid, *Protection and Control of Modern Power Systems* 5 (2) (2020) 1–15.
- [10] F. Gallardo, J. García, A. M. Ferrario, G. Comodi, J. N. Chiu, Assessing sizing optimality of OFF-GRID AC-linked solar PV-PEM systems for hydrogen production, *international journal of hydrogen energy* 47 (64) (2022) 27303–27325.
- [11] B. Pawar, E. I. Batzelis, S. Chakrabarti, B. C. Pal, Grid-forming control for solar PV systems with power reserves, *IEEE Transactions on Sustainable Energy* 12 (4) (2021) 1947–1959.
- [12] S. D. Tavakoli, M. G. Dozein, V. A. Lacerda, M. C. Mañe, E. Prieto-Araujo, P. Mancarella, O. Gomis-Bellmunt, Grid-forming services from hydrogen electrolyzers, *IEEE Transactions on Sustainable Energy* 14 (4) (2023) 2205–2219.
- [13] C. Qi, S. Qin, F. Miao, S. Li, R. Wang, Test and assessment of grid forming wind turbine based on controller hardware-in-the-loop, in: *2021 IEEE 5th Conference on Energy Internet and Energy System Integration (EI2)*, IEEE, 2021, pp. 2718–2723.
- [14] F. Zhao, X. Wang, Z. Zhou, L. Harnefors, J. R. Svensson, L. H. Kocewiak, M. P. S. Gryning, Control interaction modeling and analysis of grid-forming battery energy storage system for offshore wind power plant, *IEEE Transactions on Power Systems* 37 (1) (2021) 497–507.
- [15] Y. Zuo, Z. Yuan, F. Sossan, A. Zecchino, R. Cherkaoui, M. Paolone, Performance assessment of grid-forming and grid-following converter-interfaced battery energy storage systems on frequency regulation in low-inertia power grids, *Sustainable Energy, Grids and Networks* 27 (2021) 100496.
- [16] A. Dyśko, A. Egea, Q. Hong, A. Khan, P. Ernst, R. Singer, A. Roscoe, Testing characteristics of grid forming converters part III: Inertial behaviour, in: *19th Wind Integration Workshop*, 2020.
- [17] F. Gerini, Y. Zuo, R. Gupta, A. Zecchino, Z. Yuan, E. Vagnoni, R. Cherkaoui, M. Paolone, Optimal grid-forming control of battery energy storage systems providing multiple services: Modeling and experimental validation, *Electric Power Systems Research* 212 (2022) 108567.
- [18] Y. Qiu, B. Zhou, T. Zang, Y. Zhou, S. Chen, R. Qi, J. Li, J. Lin, Extended load flexibility of utility-scale P2H plants: Optimal production scheduling considering dynamic thermal and HTO impurity effects, *Renewable Energy* 217 (2023) 119198.
- [19] P. Marocco, D. Ferrero, M. Gandiglio, M. Ortiz, K. Sundseth, A. Lanzini, M. Santarelli, A study of the techno-economic feasibility of H₂-based energy storage systems in remote areas, *Energy Conversion and Management* 211 (2020) 112768.
- [20] P. Marocco, D. Ferrero, A. Lanzini, M. Santarelli, The role of hydrogen in the optimal design of off-grid hybrid renewable energy systems, *Journal of Energy Storage* 46 (2022) 103893.
- [21] P. Marocco, D. Ferrero, A. Lanzini, M. Santarelli, Optimal design of stand-alone solutions based on RES+hydrogen storage feeding off-grid communities, *Energy Conversion and Management* 238 (2021) 114147.
- [22] M. Gandiglio, P. Marocco, I. Bianco, D. Lovera, G. Blengini, M. Santarelli, Life cycle assessment of a renewable energy system with hydrogen-battery storage for a remote off-grid community, *International Journal of Hydrogen Energy* 47 (77) (2022) 32822–32834.
- [23] A. S. Al-Buraiki, A. Al-Sharafi, Hydrogen production via using excess electric energy of an off-grid hybrid solar/wind system based on a novel performance indicator, *Energy Conversion and Management* 254 (2022) 115270.
- [24] J. Lu, M. Li, Q. Li, Modeling and optimal design of a grid-independent solutions based on solar-hydrogen storage feeding green building by optimization algorithm, *Journal of Energy Storage* 62 (2023) 106844.
- [25] Y. W. Koholé, C. A. W. Ngouleu, F. C. V. Fohagui, G. Tchuen, Optimization of an off-grid hybrid photovoltaic/wind/diesel/fuel cell system for residential applications power generation employing evolutionary algorithms, *Renewable Energy* 224 (2024) 120131.

- [26] S. Mohseni, A. C. Brent, Economic viability assessment of sustainable hydrogen production, storage, and utilisation technologies integrated into on-and off-grid micro-grids: A performance comparison of different meta-heuristics, *International Journal of Hydrogen Energy* 45 (59) (2020) 34412–34436.
- [27] C. Xu, Y. Ke, Y. Li, H. Chu, Y. Wu, Data-driven configuration optimization of an off-grid wind/PV/hydrogen system based on modified NSGA-II and CRITIC-TOPSIS, *Energy Conversion and Management* 215 (2020) 112892.
- [28] O. L. Oyewole, N. I. Nwulu, E. J. Okampo, Optimal design of hydrogen-based storage with a hybrid renewable energy system considering economic and environmental uncertainties, *Energy Conversion and Management* 300 (2024) 117991.
- [29] I. Violo, G. Valenzuela-Venegas, M. Zeyringer, S. Sartori, A renewable power system for an off-grid sustainable telescope fueled by solar power, batteries and green hydrogen, *Energy* 282 (2023) 128570.
- [30] C. Wang, S. D. Walsh, T. Longden, G. Palmer, I. Lutalo, R. Dargaville, Optimising renewable generation configurations of off-grid green ammonia production systems considering Haber-Bosch flexibility, *Energy Conversion and Management* 280 (2023) 116790.
- [31] N. Ibagon, P. Muñoz, V. Díaz, E. Teliz, G. Correa, Techno-economic analysis for off-grid green hydrogen production in Uruguay, *Journal of Energy Storage* 67 (2023) 107604.
- [32] G. Yang, Y. Jiang, S. You, Planning and operation of a hydrogen supply chain network based on the off-grid wind-hydrogen coupling system, *International Journal of Hydrogen Energy* 45 (41) (2020) 20721–20739.
- [33] Z. Shao, X. Cao, Q. Zhai, X. Guan, Risk-constrained planning of rural-area hydrogen-based microgrid considering multi-scale and multi-energy storage systems, *Applied Energy* 334 (2023) 120682.
- [34] Y. Pang, L. Pan, J. Zhang, J. Chen, Y. Dong, H. Sun, Integrated sizing and scheduling of an off-grid integrated energy system for an isolated renewable energy hydrogen refueling station, *Applied Energy* 323 (2022) 119573.
- [35] R. Babaei, D. S. Ting, R. Carriveau, Optimization of hydrogen-producing sustainable island microgrids, *International Journal of Hydrogen Energy* 47 (32) (2022) 14375–14392.
- [36] O. Babatunde, J. Munda, Y. Hamam, Off-grid hybrid photovoltaic-micro wind turbine renewable energy system with hydrogen and battery storage: Effects of sun tracking technologies, *Energy Conversion and Management* 255 (2022) 115335.
- [37] A. Al-Sharafi, A. Z. Sahin, T. Ayar, B. S. Yilbas, Techno-economic analysis and optimization of solar and wind energy systems for power generation and hydrogen production in Saudi Arabia, *Renewable and Sustainable Energy Reviews* 69 (2017) 33–49.
- [38] Z. Abidin, N. Al Khafaf, B. McGrath, Feasibility of hydrogen hybrid energy systems for sustainable on-and off-grid integration: An australian rezs case study, *International Journal of Hydrogen Energy* 57 (2024) 1197–1207.
- [39] B. Nastasi, S. Mazzoni, Renewable hydrogen energy communities layouts towards off-grid operation, *Energy Conversion and Management* 291 (2023) 117293.
- [40] A. Ibáñez-Rioja, P. Puranen, L. Järvinen, A. Kosonen, V. Ruuskanen, J. Ahola, J. Koponen, Simulation methodology for an off-grid solar-battery-water electrolyzer plant: Simultaneous optimization of component capacities and system control, *Applied Energy* 307 (2022) 118157.
- [41] A. Ibáñez-Rioja, L. Järvinen, P. Puranen, A. Kosonen, V. Ruuskanen, K. Hynynen, J. Ahola, P. Kauranen, Off-grid solar PV-wind power-battery-water electrolyzer plant: Simultaneous optimization of component capacities and system control, *Applied Energy* 345 (2023) 121277.
- [42] Y. Zheng, S. You, C. Huang, X. Jin, Model-based economic analysis of off-grid wind/hydrogen systems, *Renewable and Sustainable Energy Reviews* 187 (2023) 113763.
- [43] X. Cheng, J. Lin, F. Liu, Y. Qiu, Y. Song, J. Li, S. Wu, A coordinated frequency regulation and bidding method for wind-electrolysis joint systems participating within ancillary services markets, *IEEE Transactions on Sustainable Energy* 14 (3) (2022) 1370–1384.

- [44] M. G. Dozein, A. Jalali, P. Mancarella, Fast frequency response from utility-scale hydrogen electrolyzers, *IEEE Transactions on Sustainable Energy* 12 (3) (2021) 1707–1717.
- [45] M. G. Dozein, A. M. De Corato, P. Mancarella, Virtual inertia response and frequency control ancillary services from hydrogen electrolyzers, *IEEE Transactions on Power Systems* 38 (3) (2022) 2447–2459.
- [46] R. Rosso, X. Wang, M. Liserre, X. Lu, S. Engelken, Grid-forming converters: Control approaches, grid-synchronization, and future trends—a review, *IEEE Open Journal of Industry Applications* 2 (2021) 93–109.
- [47] R. H. Lasseter, Z. Chen, D. Pattabiraman, Grid-forming inverters: A critical asset for the power grid, *IEEE Journal of Emerging and Selected Topics in Power Electronics* 8 (2) (2019) 925–935.
- [48] Á. Iribarren, D. Elizondo, E. L. Barrios, H. Ibaiondo, A. Sanchez-Ruiz, J. Arza, P. Sanchis, A. Ursúa, Dynamic modeling of a pressurized alkaline water electrolyzer: A multiphysics approach, *IEEE Transactions on Industry Applications* 59 (3) (2023) 3741–3753.
- [49] M. Farrokhhabadi, S. König, C. A. Cañizares, K. Bhattacharya, T. Leibfried, Battery energy storage system models for microgrid stability analysis and dynamic simulation, *IEEE Transactions on Power Systems* 33 (2) (2017) 2301–2312.
- [50] MathWorks, Two-level converter (2024).
URL <https://ww2.mathworks.cn/help/sps/powersys/ref/threelevelnpcconverter.html>
- [51] Y. Zeng, Y. Qiu, J. Zhu, S. Chen, B. Zhou, J. Li, B. Yang, J. Lin, Scheduling multiple industrial electrolyzers in renewable p2h systems: A coordinated active-reactive power management method, *IEEE Transactions on Sustainable Energy*, Early Access.
- [52] Z. Yu, J. Lin, F. Liu, J. Li, Y. Zhao, Y. Song, Y. Song, X. Zhang, Optimal sizing and pricing of grid-connected renewable power to ammonia systems considering the limited flexibility of ammonia synthesis, *IEEE Transactions on Power Systems* 39 (2) (2023) 3631–3648.
- [53] U. K. Debnath, I. Ahmad, D. Habibi, Quantifying economic benefits of second life batteries of gridable vehicles in the smart grid, *International Journal of Electrical Power & Energy Systems* 63 (2014) 577–587.
- [54] L. Lam, P. Bauer, Practical capacity fading model for Li-ion battery cells in electric vehicles, *IEEE Transactions on Power Electronics* 28 (12) (2012) 5910–5918.
- [55] R. Mandal, K. Chatterjee, Frequency control and sensitivity analysis of an isolated microgrid incorporating fuel cell and diverse distributed energy sources, *International Journal of Hydrogen Energy* 45 (23) (2020) 13009–13024.
- [56] W. Murray, M. Adonis, A. Raji, Voltage control in future electrical distribution networks, *Renewable and Sustainable Energy Reviews* 146 (2021) 111100.
- [57] Power | Data Access Viewer.
URL <https://power.larc.nasa.gov/data-access-viewer/>
- [58] M. David, C. Ocampo-Martínez, R. Sánchez-Peña, Advances in alkaline water electrolyzers: A review, *Journal of Energy Storage* 23 (2019) 392–403.